



**HAL**  
open science

## Evidence for crustal seismic anisotropy at the InSight lander site

Jiaqi Li, Caroline Beghein, James Wookey, Paul Davis, Philippe Lognonné, Martin Schimmel, Eleonore Stutzmann, Matthew Golombek, Jean-Paul Montagner, William Bruce Banerdt

► **To cite this version:**

Jiaqi Li, Caroline Beghein, James Wookey, Paul Davis, Philippe Lognonné, et al.. Evidence for crustal seismic anisotropy at the InSight lander site. *Earth and Planetary Science Letters*, 2022, 593, 10.1016/j.epsl.2022.117654 . insu-03918195

**HAL Id: insu-03918195**

**<https://insu.hal.science/insu-03918195v1>**

Submitted on 2 Jan 2023

**HAL** is a multi-disciplinary open access archive for the deposit and dissemination of scientific research documents, whether they are published or not. The documents may come from teaching and research institutions in France or abroad, or from public or private research centers.

L'archive ouverte pluridisciplinaire **HAL**, est destinée au dépôt et à la diffusion de documents scientifiques de niveau recherche, publiés ou non, émanant des établissements d'enseignement et de recherche français ou étrangers, des laboratoires publics ou privés.

1 **Evidence for Crustal Seismic Anisotropy at the InSight Lander Site**

2

3 Jiaqi Li<sup>1\*</sup>, Caroline Beghein<sup>1</sup>, James Wookey<sup>2</sup>, Paul Davis<sup>1</sup>, Philippe Lognonné<sup>3</sup>, Martin Schimmel<sup>4</sup>,  
4 Eleonore Stutzmann<sup>3</sup>, Matthew Golombek<sup>5</sup>, Jean-Paul Montagner<sup>3</sup>, William Bruce Banerdt<sup>5</sup>

5

6

7 <sup>1</sup> Department of Earth, Planetary, and Space Sciences, University of California, Los Angeles, CA 90095, USA.

8 E-mail: [jli@epss.ucla.edu](mailto:jli@epss.ucla.edu)

9 <sup>2</sup> School of Earth Sciences, University of Bristol, Bristol, UK.

10 <sup>3</sup> Université de Paris, Institut de physique du globe de Paris, CNRS, Paris, F-75005, France.

11 <sup>4</sup> Geosciences Barcelona - CSIC, Barcelona, Spain.

12 <sup>5</sup> Jet Propulsion Laboratory, California Institute of Technology, Pasadena, CA 91109, USA.

13

14

15

16

17

18

19

20

# 21 Abstract

22 We analyzed broadband and low-frequency events recorded on Mars and made the first detection of horizontally  
23 polarized shear wave reflections, which help constrain the crustal structure at NASA's InSight lander site. Coherent  
24 signals from five well-recorded marsquakes appear to be independent of the focal depth and are consistent with SH-  
25 wave reflections off the topmost crustal interface ( $8 \pm 2$  km). This phase confirms the existence of the  $\sim 8$  km interface  
26 in the crust and the large wave speed (or impedance) contrast across it. The range of acceptable parameters determined  
27 from the detected SH-wave reflections differs from the majority of the vertically polarized shear wave models  
28 resulting from a previous receiver function study, indicating that the velocity of the vertically polarized waves, is  
29 larger than that of horizontally polarized waves. We propose that this inconsistency results from the presence of  
30 seismic anisotropy within the top crustal layer at the lander site. Modeling results show that dry- or liquid-filled  
31 cracks/fractures and igneous intrusions can reproduce the observed radial anisotropy.

32

33

34

35 **Keywords** martian crust, SH-wave reflections, negative radial anisotropy

36

37

38

39

40

# Introduction

Martian crustal structure can reveal how the planet differentiated and evolved over geological times (Hauck and Phillips, 2002; Plesa et al., 2018). After the landing of NASA's InSight mission (Fig. 1a) in November 2018 (Banerdt et al. 2020), data from the Seismic Experiment for Interior Structure (SEIS, Lognonné, et al., 2019) were collected and hundreds of events have been recorded. Recent receiver function (hereafter, RF) studies (Lognonné et al., 2020; Knapmeyer-Endrun et al., 2021) and autocorrelation analyses (Compaire et al., 2021; Schimmel et al., 2021; Knapmeyer-Endrun et al., 2021) provide constraints on the crustal thickness and structure beneath the InSight landing site. It was shown that it is characterized by interfaces at  $8 \pm 2$  km and  $20 \pm 5$  km depth. A third interface may also be present at  $39 \pm 8$  km depth, implying two possible crustal thicknesses. Although the methods employed were effective at providing the first seismic model of the martian crust, finding additional seismic phases would help reduce the size of the model space, further constrain the crustal thickness, and possibly reveal new features.

Following the direct S-wave generated by teleseismic events, observable phases include reflected waves bouncing between the free surface and crustal discontinuities on both the source- and the receiver-side. For horizontally polarized incoming S-waves (SH) (Fig. 1c), there are no P-wave transmissions on horizontal discontinuities and SH-wave reflections are the dominant phases on the tangential component of the seismogram. On Earth, these topside SH-reverberations were utilized to image discontinuities in the upper mantle (Shearer and Buehler, 2019) and the lithosphere (Liu and Shearer, 2020). The differential travel-time between the direct SH phase (Ss) and the SH-wave reflection (SsSs) can be used to constrain the S-wave speed and thickness of the layer based on ray theory:

$$T_{SsSs-Ss} = 2H \left( \frac{1}{V_{SH}^2} - p_{SH}^2 \right)^{1/2} \quad (1)$$

where  $p_{SH}$  is the horizontal slowness (ray parameter) of the incident SH-wave,  $V_{SH}$  is the average SH-wave speed in the layer, and  $H$  is the overall thickness of that layer.

62 Compared with the more widely used RF methods (e.g., Langston 1979), SH-wave reflections can better constrain  
63 the depth of the reflector due to the relatively larger travel time differences (Liu and Shearer, 2020). In addition,  
64 unlike the RF technique, which is sensitive to the wave speed ratio between P- and SV-waves (vertically polarized  
65 shear waves), SH-wave reflections can directly constrain absolute SH-wave speeds.

66 In this paper, we focus on the shallow layer, at  $8 \pm 2$  km (Lognonné et al., 2020, Knapmeyer-Endrun et al., 2021)  
67 of the martian crust at the lander site, hereafter referred to as Layer 1. Not only is this layer the least contaminated  
68 by interferences from source-side scattering and other reflections from deeper layers (see section 3.1), but the  
69 previously observed large wave speed jump at the interface (up to +40%, Knapmeyer-Endrun et al. (2021)) can  
70 generate strong reflected phases that are observable with a single event without the need for stacking. In addition,  
71 any constraints on Layer 1 would provide useful information for future studies on the deeper layers.

72

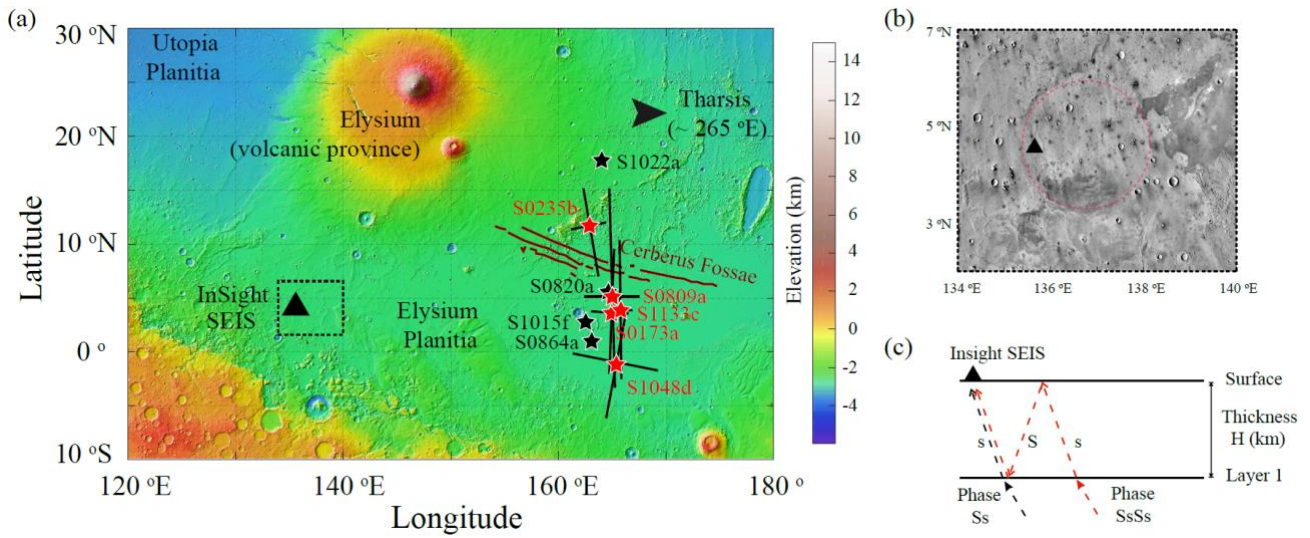
## 73 **Data and Methods**

74 From Sol 105, when the first low-frequency marsquake was recorded by SEIS, to Sol 1133, a total of 86 broadband  
75 and low-frequency events were detected (Clinton et al., 2021; InSight Marsquake Service, 2020, 2021a, b, 2022a, b).  
76 Eleven of them are rated as quality-A, as defined by Clinton et al. (2021), with constraints on both their epicentral  
77 distance and back azimuth. We analyzed the waveforms (InSight Mars SEIS Data Service, 2019) from all the quality-  
78 A marsquakes with epicentral distances smaller than 60 degrees (9 out of 11, see Table S1) to avoid interferences  
79 with mantle triplications generated by the olivine-to-wadsleyite phase transition that occurs at around 1000 km depth  
80 on Mars (Stähler et al., 2021).

81 We note that since the SEIS instrument operates in an extremely harsh environment (both wind and temperature,  
82 e.g., Lognonné et al. 2020, Ceylan et al. 2021), internal thermal stresses from diurnal temperature variations can

83 generate transient one-sided pulses, hereafter referred to as glitches (Scholz et al., 2020). To minimize their effect,  
 84 we hierarchically detected the glitches in the continuous waveform and removed them on the U, V, W components  
 85 using a synthetic glitch template (Scholz et al., 2020).

86



87

88

Figure 1.

89

90

91

92

93

94

95

- (a) Topographic map from Mars Orbiter Laser Altimeter (MOLA, Smith et al., 2001) near the InSight lander (black triangle). The red and black stars mark the nine quality-A events selected for this study. The red stars denote the five marsquakes used in the inversion and the black error-bars indicate the uncertainties in both their epicentral distance and back azimuth. The black stars show the other four quality-A events.
- (b) Mars Orbiter Laser Altimeter digital elevation map overlain on infrared daytime image from the Thermal Emission Imaging System (THEMIS-IR, Edwards et al. 2011) of the region (marked by dashed box) in (a). The quasi-circular depression, interpreted to be a buried, degraded impact crater (~175 km diameter) is indicated by the dotted red circle, with the InSight lander (black triangle) near the western edge of the crater (Golombek et al., 2018).
- (c) Ray paths of the SH-wave reflection from a planar, incident teleseismic SH-wave near the InSight SEIS instrument. The direct phase Ss is in black and the reflected phase is in red.

96

97 For the deglitched dataset (provided as supplementary data), which had a sampling rate of 20 samples per second,

98 we removed the instrument response, with a pre-filtering from 0.01 to 8 Hz, to get the ground motion records. To

99 analyze SH-wave reflections, we need to use data on the tangential (T) component. We thus rotated the coordinates

100 from the original UVW to NEZ using ObsPy (Beyreuther et al., 2010), which required back azimuth information.  
101 Because the back azimuth is also defined as the angle to rotate the N and E components into R and T components,  
102 we estimated its value based on the analysis of P-wave polarization with data filtered from 2 s to 5 s (Fig. 2 and Fig.  
103 3). For these nine quality-A events, our derived back azimuths are all within the estimated ranges from the InSight  
104 Marsquake Service (MQS) (2020, 2021a, b, 2022a, b). We further tested that uncertainties in the back azimuth do not  
105 influence our SH-wave arrivals (see section 3.2 and Fig. S1).

## 106 1.1 Data Analysis

107 In the present study, we calculated synthetic SH waveforms (on the tangential component) for all 40,000 most likely  
108 P-wave RF crustal models obtained by Knapmeyer-Endrun et al. (2021). The synthetics were calculated with the  
109 propagator matrix method (Kennett, 2009) using ray parameters estimated from the Mars mantle model of Stähler et  
110 al. (2021). Synthetic waveforms indicate that the predicted SH-wave reflection off Layer 1 has a negative polarity  
111 compared to the direct SH phase, and arrives at around  $9.5 \pm 1.5$  seconds for events with epicentral distances of  
112 about 30 degrees (e.g., see Fig. 4a2). Thus, for the data, we aligned and normalized the T-component seismogram  
113 according to the direct SH phase (multiplied by -1 to make the polarity of the direct SH phase positive, if needed) for  
114 each event, and searched for a negative phase (Shearer, 2019) in a wider time-window of  $9.5 \pm 3.0$  seconds. We  
115 note that we chose a relatively broad filtering band to maintain the original appearance of the data as much as possible.

116 Out of the nine selected events, five (S0235b, S1133c, S0173a, S1048d, and S0809a) display clear negative phases  
117 indicative of SH reflections off Layer 1. For instance, broadband event S0235b (Fig. 2a1) shows a clear negative  
118 signal at around 10.2 s after the direct SH phase. It also displays complexity in the source time function over a broad  
119 frequency range (from 30 s to 3 Hz) with two separate positive phases of different amplitudes at -5 s and 0 s. If we  
120 shift the original trace (the black waveform in Fig. 2a1 and Fig. 2a2) by 10.2 s and amplify its amplitude by -300%

121 (the red waveform in Fig. 2a2), the phase originally at 10.2 s fits the source wavelet (from -1 to 1 s) very well (with  
122 a cross-correlation coefficient of 0.92). We note that a negative amplification factor (i.e., -300%) accounts for the  
123 polarity change for the topside SH-reflection off Layer 1 (Shearer, 2019). More surprisingly, the entire complex  
124 source wavelet (from -5 to 2 s) is well-matched (with a cross-correlation coefficient of 0.75). This similarity with the  
125 source wavelet indicates that this negative signal at around 10 s, on the tangential component, is likely a reflected  
126 phase, generated either at the receiver side or the source side.

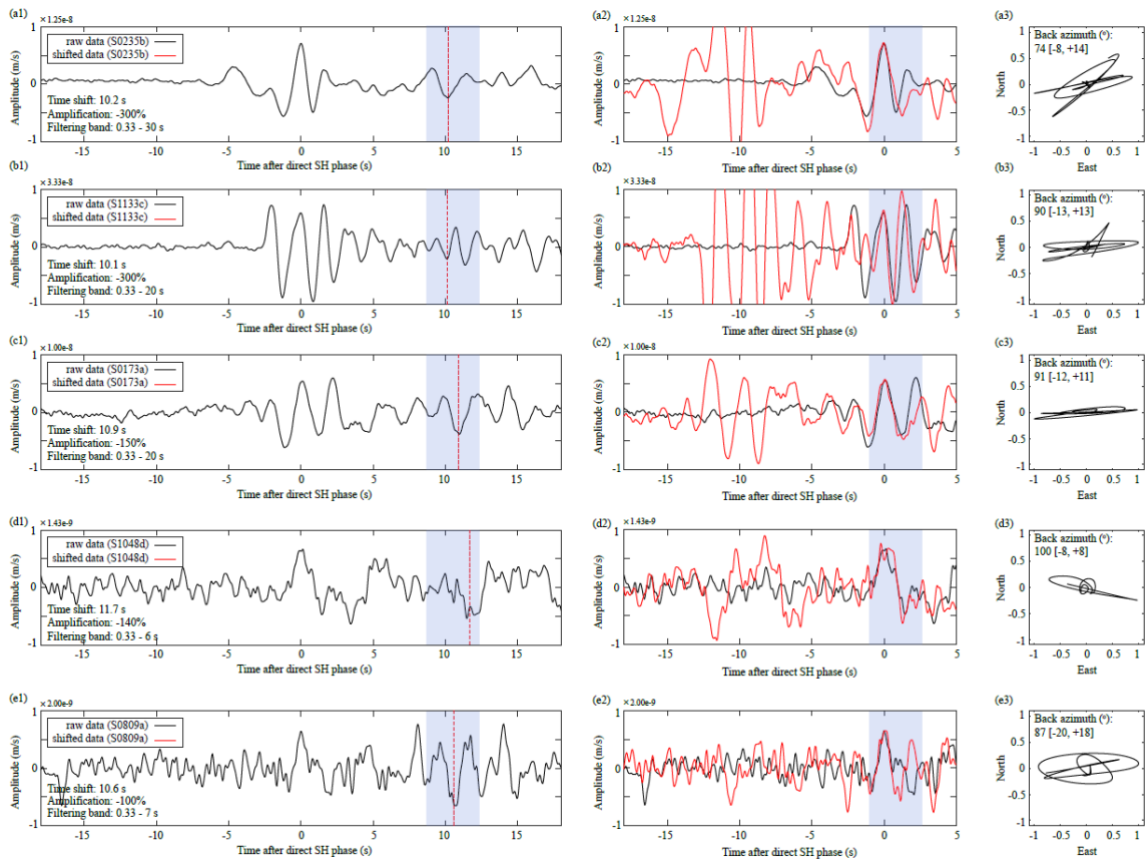
127 For broadband event S1133c, there is also a clear signal at around 10 s. When a similar time shift of 10.1 s and an  
128 amplification factor of -300% is applied to the original trace (Fig. 2b), the direct SH-phase (although with multiple  
129 peaks) can be matched with a cross-correlation coefficient of 0.71. Low-frequency event S1048d (from 6 s to 3 Hz,  
130 see Fig. 2d) also exhibits a negative phase at around 11.7 s, although there is another positive signal at around 5 s  
131 which might be the depth phase from the source side (see Discussion). Nevertheless, this positive signal at around 5  
132 s does not interfere with the negative phase at around 11.7 s, and the similarity between the negative phase (at around  
133 11.7 s) and the source wavelet (from -1 to 3 s) is high (with cross-correlation coefficient of 0.89). Low-frequency  
134 events S0173a (from 30 s to 3 Hz, see Fig. 2c) and S0809a (from 7 s to 3 Hz, see Fig. 2e) coherently show negative  
135 phases at 10.9 s and 10.6 s, respectively. However, besides a positive phase at around 5 s (like S1048d), there are  
136 other pulses between 10 s and 15 s which will probably be overlapped with the negative phase at around 11 s.

137 The other four quality-A events (S1015f, S1022a, S0864a, and S0820a) exhibit hints of negative phases at similar  
138 arrival times as the events discussed above and do not violate the observations. However, they generally behave less  
139 well. For broadband event S1015f (Fig. 3a), the possible source wavelet is too complex (including four phases at -3  
140 s, 0 s, 2 s, and 4 s): although the last three source wavelets can be matched by the negative wave trains beginning at  
141 around 10.7 s, the corresponding reflected phase for the first source wavelet (-3 s) cannot be found and is probably  
142 buried in the long source time function (duration of about 10 s). Low-frequency event S1022a (Fig. 3b) displays a

143 lack of high-frequency energy, and broadband event S0864a (Fig. 3c) as well as low-frequency event S0820a (Fig.  
144 3d) present strong oscillations after the direct SH waves.

145 To summarize, S0235b is the best event among all nine quality-A events, with a clear negative phase at 10.2 s, and  
146 there are no other phases in between. Events S1133c, S0173a, S1048d, and S0809a also show a consistent negative  
147 phase at 10 s to 12 s, although the source wavelets for S1133c and S0173a display multiple peaks that hinder the  
148 waveform matching. There is also contamination from noise or other unknown phases which might affect the  
149 amplitude and arrival time. Events S1015f, S1022a, S0864a, and S0820a display similar negative phases, but they  
150 were discarded due to their lower quality regarding the detection of the SH reflected waves. Because the negative  
151 phase observation at around 10 s to 12 s is consistent for all nine quality-A events, it is more likely to come from a  
152 common crustal structure (Layer 1) at the receiver side than to reflect a common focal depth for all these events (see  
153 section 3.1).

154 We note that the different behavior of the quality-A events is understandable because event quality was defined in  
155 terms of the performance regarding event location (Clinton et al., 2021). Specifically, achieving quality-A requires  
156 both clear P and S phases and polarization, yielding clear epicentral distance and back azimuth, respectively.  
157 Therefore, the definition of a quality-A event takes only the direct S phase into account, and does not consider the  
158 source time function (e.g., S1015f and S1022a), possible depth phases (e.g., S0173a, S0809a, and S1048d), or  
159 oscillations after the direct phase (e.g., S0820a and S0864a).



160

161

162

163

Figure 2. Waveforms for events S0235b, S1133c, S0173a, S1048d, and S0809a.

(a1) The black waveform is the velocity data for event S0235b on the tangential (T) component. The shaded purple region and the dashed red line mark the arrival of the negative signal at 10.2 s. The filtering band is denoted in the lower left corner.

(a2) Comparison between the original waveform (in black), and the shifted trace (by -10.2 s) with its amplitude amplified by -300% (in red). With a time shift and amplitude amplification, the negative phase (originally at 10.2 s) overlaps with the source wavelet.

(a3) P-wave particle motion (black curves) for event S0235b (in a 6-s time window around the direct P-wave arrival). The back azimuth and its uncertainties from MQS (Clinton et al., 2021; InSight Marsquake Service, 2021a, b, 2022) are denoted in the upper left corner.

Same analysis for event (b1-b3) S1133c, (c1-c3) S0173a, (d1-d3) S1048d, and (e1-e3) S0809a.

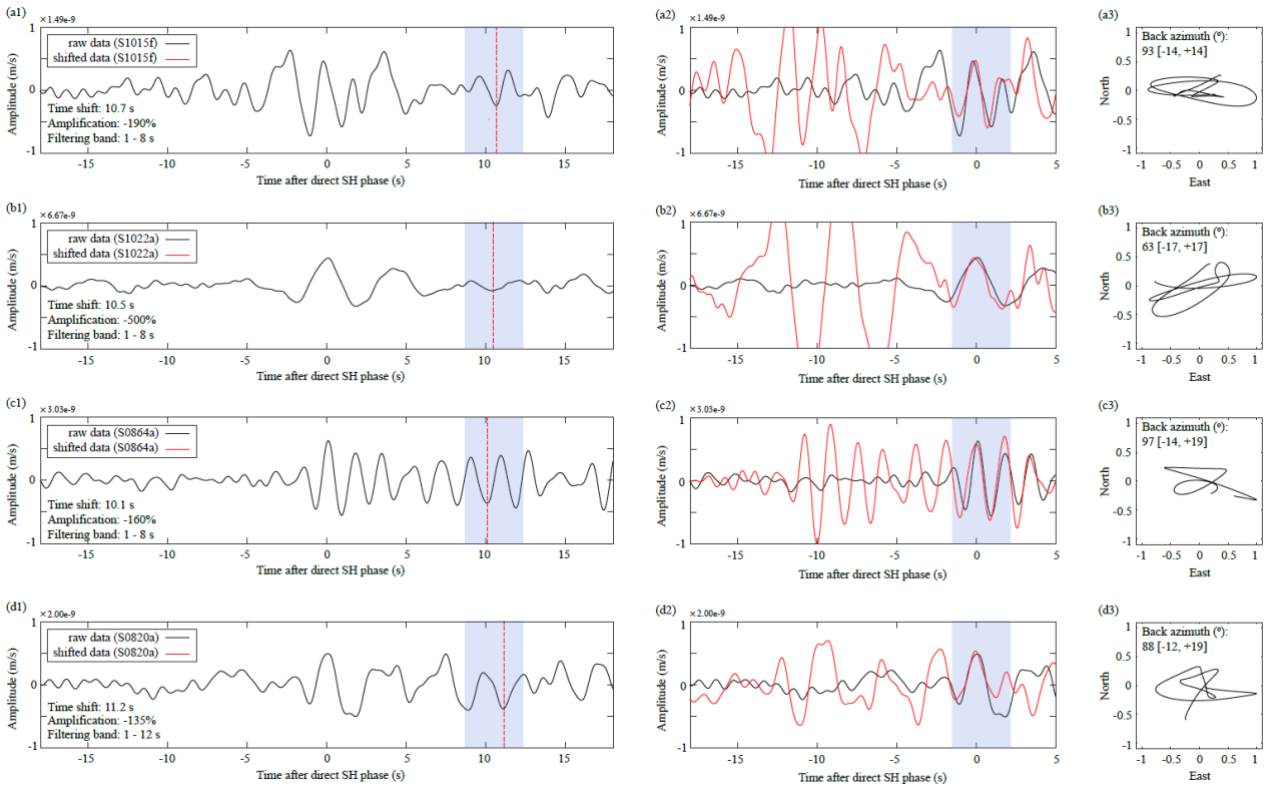


Figure 3. Waveforms for events (a1-a3) S1015f, (b1-b3) S1022a, (c1-c3) S0864a, and (d1-d3) S0820a. The layout is the same as Fig. 2.

## 1.2 Constraints from SH-wave reflections

We focus on waveforms from events S0235b, S1133c, S0173a, S1048d, and S0809a to constrain the SH-wave speed and thickness of Layer 1. For the synthetic seismogram, since each event has a distinct source time function, we convolved the original synthetic output (delta function as the source wavelet) with the assumed source wavelet (from -7 to 3 s of the data).

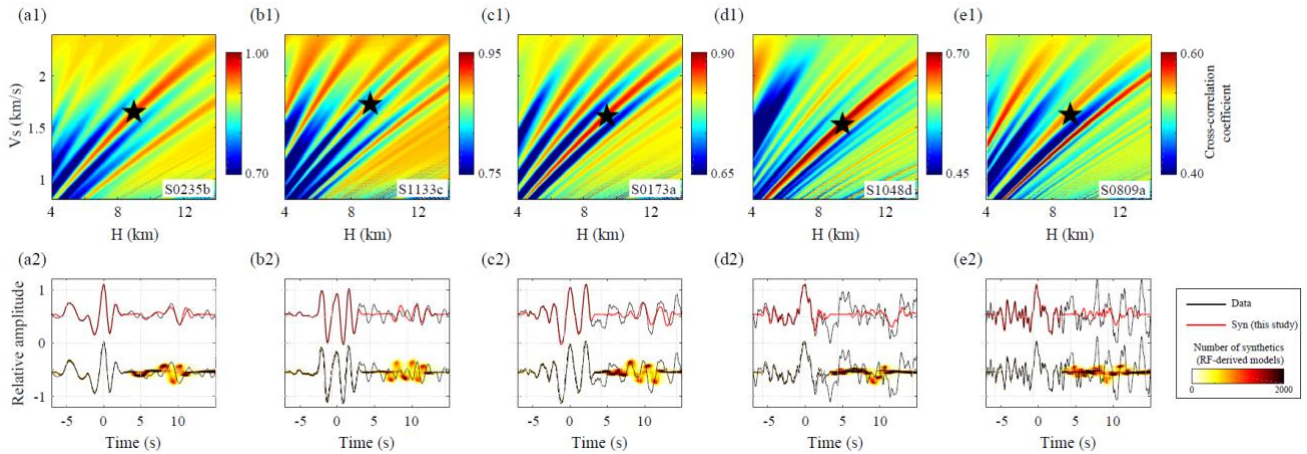


Figure 4. Cross-correlation coefficients for combinations of SH-wave velocity and layer thickness and comparison between observations and synthetic waveforms.

(a1) Cross-correlation map for event S0235b. The black star marks the model used to calculate the synthetics in (a2).

(a2) The two traces at the top are the data (in black) and the synthetics (in red, the corresponding model is indicated by the black star in a1) for event S0235b on the tangential (T) component. The two traces at the bottom are the data (in black) and the synthetics (color scales denote the number of models) calculated using 40,000 models from the RF study (Knapmeyer-Endrun et al. 2021). Same analysis for event (b1-b3) S1133c, (c1-c3) S0173a, (d1-d3) S1048d, and (e1-e3) S0809a.

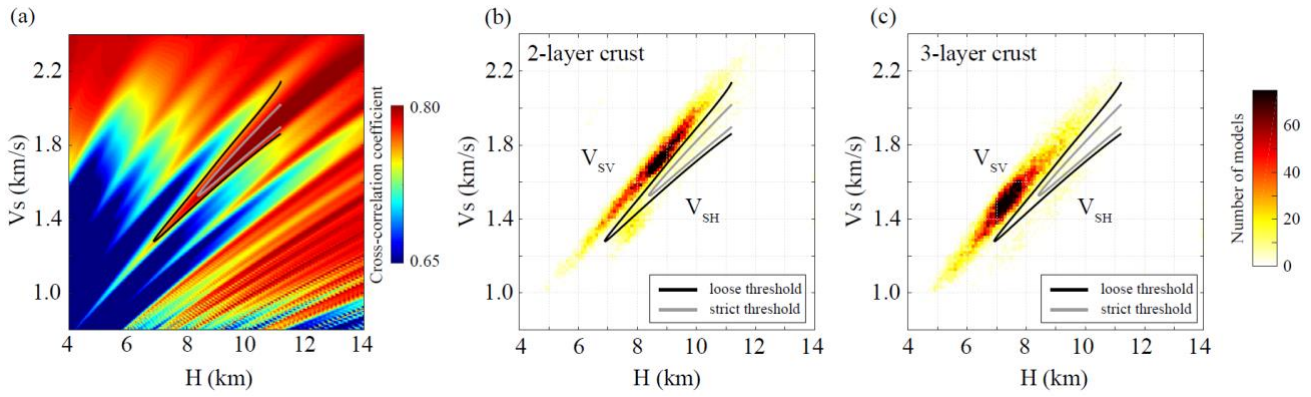
Equation (1) shows that trade-offs exist between model parameters (SH-wave speed and thickness of Layer 1) and therefore the solution is non-unique. To find all acceptable models, we sampled the SH-wave speed (from 0.8 km/s to 2.4 km/s with an interval of 0.01 km/s) and thickness (from 4 km to 14 km with an interval of 0.05 km) of Layer 1. At each grid cell, we calculated synthetic waveforms, convolved the synthetics with their source wavelet, and finally derived the cross-correlation coefficient between the data and the synthetics. The cross-correlation maps are shown in the top panels of Fig. 4. Models in the red regions have higher cross-correlation coefficients and are thus more acceptable than models in the blue regions. One of those models was selected (represented by the black star) and the corresponding waveform is shown in the bottom panels of Fig.4 to illustrate that they predict waveforms that are similar to the data. The cross-correlation maps for these five events are similar, especially the first-order pattern. They all show a sub-linear region on the diagonal, consistent with the ray-theory-based equation (1). We note that there are multiple red regions in the cross-correlation maps for S1133c (Fig. 4b1) and S0173a (Fig. 4c1). Those

192 features are due to the multiple peaks in the source time functions of those two events, which are not observed in  
193 other events with relatively simple source time functions. Other differences between the cross-correlation maps might  
194 be partly due to different noise levels, frequency bands, source-side scattering, epicentral distances, and possible  
195 interference from other phases.

196 To enhance the coherent features, we summed these cross-correlation maps with different weights (see Discussion).  
197 The weights for S0235b, S1133c, S0173a, S1048d, and S0809a are 1.0, 0.2, 0.2, 0.5, and 0.2, respectively. We note  
198 that events S1133c, S0173a, S1048d, and S0809a are down-weighted because of multiple peaks in the source wavelet  
199 or interferences from other phases, and events S1133c, S0173a, and S0809a are further down-weighted due to their  
200 similar back azimuths. The summed cross-correlation map is shown in Fig. 5a. To extract the acceptable region of  
201 the model space (the red region on the diagonal), we set both a strict cross-correlation coefficient threshold of 0.785  
202 (the grey curve in Fig. 5a) and a slightly looser threshold of 0.765 (the black curve in Fig. 5a). We note that we did  
203 not pick the arrival time of the phases nor did we use equation (1) to calculate the corresponding wave speed and the  
204 layer thickness. Instead, we chose the threshold of the cross-correlation map to extract acceptable model regions.  
205 Cross-correlation maps are more reliable to measure travel time differences since multiple sources of uncertainties,  
206 such as the noise in the data, the duration of the pulse, and even finite-frequency effects, are automatically included.

207 We tested several thresholds and compared them with predictions from ray theory to ensure our analyses are  
208 reliable. We found that if we consider a value smaller than 0.765, the contour (Fig. S2c) begins to significantly deviate  
209 from the trend along the diagonal and is inconsistent with the prediction from equation (1).

210



211

212

Figure 5. S-wave speed models for Layer 1.

213

(a) Summed cross-correlation map for the SH-wave reflections. The black and grey curves mark the acceptable model regions with loose and strict thresholds, respectively.

214

(b) Colored dots represent the 20,000 models from the receiver functions study (Knapmeyer-Endrun et al., 2021) for the 2-layer crustal case. Color indicates the number of models at each grid point.

(c) Same as (b) for the 3-layer crustal case.

215

216

## Results

217

### 2.1 S-wave speed

218

Our study provides constraints on SH-wave velocity using SH-wave reflections, which can be compared to the

219

20,000 acceptable 2-layer and 3-layer crustal models of the Knapmeyer-Endrun et al. (2021) RF study. Here, we

220

plotted the distribution of S-wave speed and thickness for the top layer using those 20,000 models in the 2-layer and

221

3-layer models obtained with RF (Fig. 5b and 5c, respectively). In both cases, the models are roughly located along

222

a sub-linear trend reflecting the trade-offs between the wave speed and layer thickness.

223

Assuming the P-to-s converted phases (from the RF study) and the SH-wave reflections are generated from the

224

same interface (discussion of this assumption can be found in section 3.3), we superimposed the acceptable model

225

space regions determined from our SH-wave reflections analysis for the strict and loose thresholds (e.g., grey and

226 blue lines in Fig. 5b, respectively). Results show that the range of acceptable parameters determined from our SH-  
227 wave analysis does not intersect with the majority of the 20,000 models from Knapmeyer-Endrun et al. (2021), for  
228 both the strict and loose thresholds. More specifically, for each layer thickness, the acceptable S-wave speeds from  
229 the SH-wave reflections are systematically lower than those from the RF study. Consistently, the predicted arrival  
230 times (at around 9 seconds) with the RF-derived models (the bottom panels of Fig. 4) are also earlier than the signals  
231 we observed at around 11 seconds.

232 We propose that this inconsistency results from the presence of seismic anisotropy within crustal Layer 1 at the  
233 lander site since our SH-wave reflections study constrains horizontally polarized shear-wave velocity ( $V_{SH}$ ) whereas  
234 the RFs analysis constrains vertically polarized shear-wave speed ( $V_{SV}$ ).

235 For the best event, S0235b, a delay time of 10.2 s, and amplification of -300% are required to match the reflected  
236 phase and the direct SH-wave. For the other four events, either complex source wavelets are observed (i.e., S1133c,  
237 and S0173a) or very different and suspiciously low amplifications are required (i.e., S0173a, S1048d, and S0809a).  
238 Although low weights for the other four events were set during the inversion (Fig. 5a), we performed an additional  
239 inversion using only the single event S0235b. Despite the differences in the absolute values of the cross-correlation  
240 coefficients, both inversions yield very similar results of  $V_{SH} < V_{SV}$  (Fig. 5 and Fig. S3). We also note that most of the  
241 other events show larger travel time differences (i.e., 10.1, 10.6, 10.9, and 11.7 s) compared with S0235b (i.e., 10.2  
242 s). Consequently, the currently derived value of  $V_{SH}$  (where other events have low weights) can be viewed as a  
243 maximum estimation. Therefore, applying different weights (e.g., enlarging the weights for other events) will even  
244 lower the value of  $V_{SH}$  without changing the conclusion of  $V_{SH} < V_{SV}$  (Fig. S4).

## 245 2.2 Crustal Anisotropy

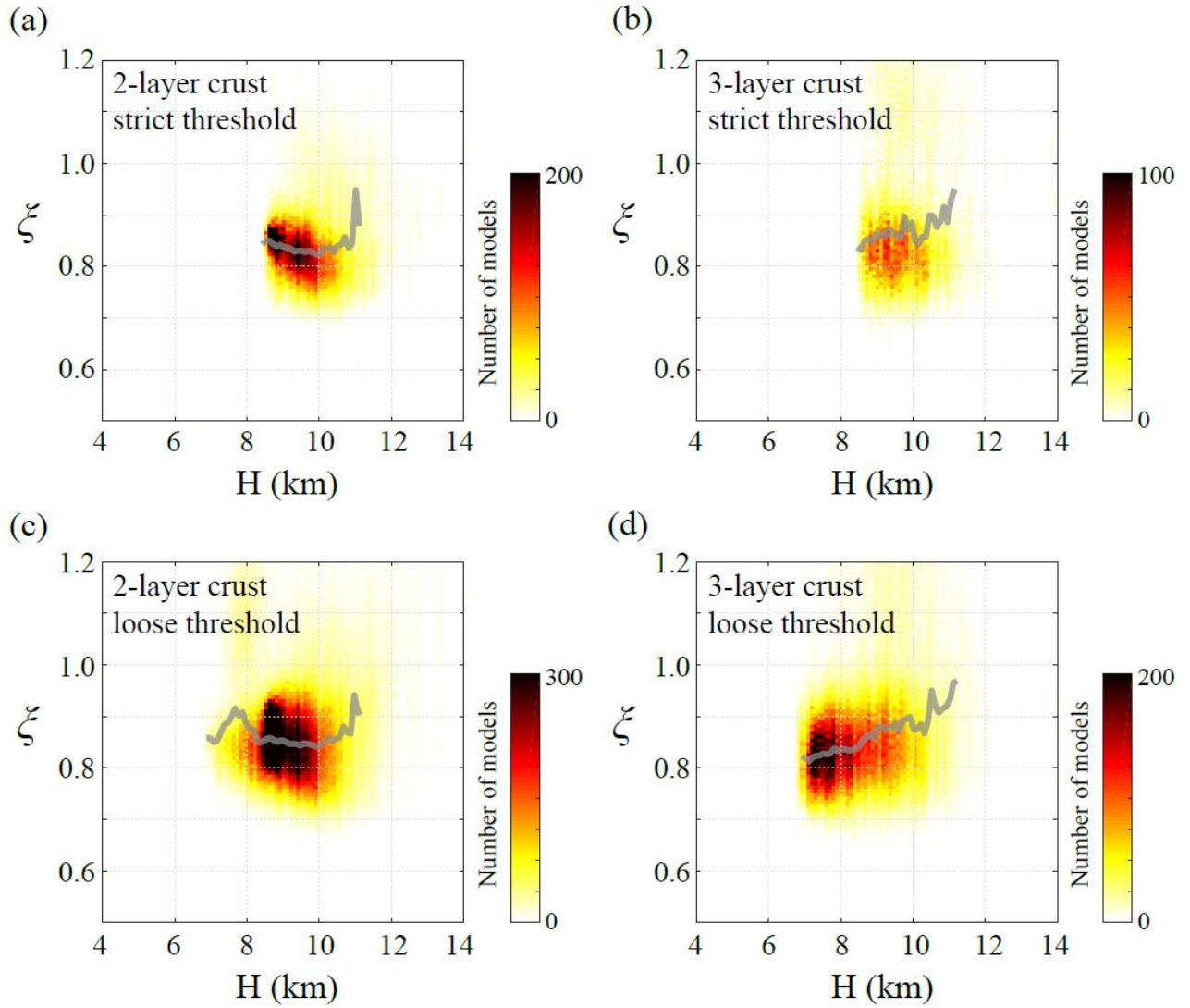
246 To quantify the radial anisotropy amplitude, we sampled the  $V_{SV}$  and  $V_{SH}$  models to calculate the anisotropy coefficient

247  $\xi = (V_{SH}/V_{SV})^2$ . In practice, we first extracted  $V_{SV}$  and layer thickness of the model at each grid point. Then, for this  
248 specific layer thickness, we sampled  $V_{SH}$  between its upper and lower limits (i.e., grey and blue lines for the strict  
249 and loose thresholds in Fig. 5a, respectively) with an interval of 0.01 km/s and calculated the corresponding  $\xi$  values.  
250 We did this for all the model grids and derived  $\xi$  distribution maps. Fig. 6a and 6b show the  $\xi$  distributions with  
251 the strict  $V_{SH}$  threshold for the 2-layer and 3-layer crust cases, respectively. Similar maps for the loose  $V_{SH}$  threshold  
252 are shown in Fig. 6c and 6d. For all cases, the  $\xi$  values are concentrated between 0.7 and 0.9, corresponding to  
253  $V_{SH} < V_{SV}$  with 10% to 30% anisotropy. The mean value and standard deviation of  $\xi$  are 0.88 and 0.10, respectively.

254 In addition to choosing the thickness from the RF models, we performed an additional calculation in which we  
255 performed a grid search for all the possible thickness values (with an interval of 0.1 km) and then calculated the  
256 anisotropy coefficient for each thickness using the averaged  $V_{SV}$  and  $V_{SH}$  values from the RF and SH-wave reflection  
257 studies, respectively. The average coefficient value (the solid grey curves in Fig. 6) is around 0.85, which falls into  
258 the previous range between 0.7 and 0.9.

259 To determine the reliability of our threshold choices, we tried to find a threshold value in the SH-wave reflection  
260 cross-correlation map (Fig. 5a) that would force  $V_{SH}$  to be equal to  $V_{SV}$ . We found that we would need a threshold  
261 lower than 0.65, which deviates significantly from the predictions of ray theory (Eq. 1). We, therefore, conclude that  
262 an isotropic layer is less likely than our solution with  $V_{SH} < V_{SV}$ .

263



264

265

Figure 6. Radial anisotropy coefficient  $\xi = (V_{SH}/V_{SV})^2$  in Layer 1.

266

(a) Distribution of the radial anisotropy coefficient for the 2-layer crustal case in the receiver functions study (Knapmeyer-Endrun et al., 2021) with the strict SH-wave threshold. The color scale indicates the number of models at each grid point. The solid grey line mark the average value of the anisotropy coefficient.

267

(b) The 3-layer crustal case with the strict SH-wave threshold.

268

(c) The 2-layer crustal case with the loose SH-wave threshold.

(d) The 3-layer crustal case with the loose SH-wave threshold.

269

## 270 **Discussion**

### 271 **3.1 Source-side scattering**

272 Our target structure is the top crustal layer (at  $8 \pm 2$  km depth) beneath the InSight lander. At the receiver side, any  
273 free-surface reflections from deeper layers will arrive later and thus fall outside of the window of interest. The only  
274 phases that may arrive earlier are the waves reflected between Layer 1 and the deeper layer (at  $20 \pm 5$  km depth), but  
275 the amplitudes of such inter-layer reflections are much smaller than reflections at the free surface (Fig. S5). Therefore  
276 receiver-side reflections from deeper layers do not influence our phase identification or the results presented in this  
277 study.

278 Interference, if present, would come from the source side. When the focal depth is shallower or closer to the  
279 discontinuity, free-surface reflection at the source side yields similar arrival times as receiver-side reflections (e.g.,  
280 the SH-wave reflections we studied in this paper). Therefore, deep events are usually preferred for SH-wave reflection  
281 studies (Liu and Shearer, 2020). Although there have not yet been conclusive focal depth reports for marsquakes due  
282 to the unclear identification of depth phases, most of the detected low-frequency and broadband events are likely  
283 deeper than Layer 1 since they do not excite trapped waves (Giardini et al., 2020). Therefore, the possible source-  
284 side scattering will not likely arrive at similar times as the receiver-side SH-wave reflections for Layer 1, but the  
285 depth of Layer 1 at the source side may differ from the one beneath the SEIS station.

286 Nevertheless, all events with clear negative signals show coherent arrivals at around 10-11 s (Figs. 2 and 3). This  
287 consistency implies that the phases we interpreted to be the SH-wave reflections are not strongly dependent on the  
288 focal depths. If the negative phase was a depth phase, all events with different locations (Fig. 1a) would have to have  
289 similar focal depths and focal mechanisms to ensure coherent arrival times and polarity. Although we cannot

290 completely rule out this possibility, we think this is less likely since, for example, Brinkman et al. (2021) showed that  
291 focal mechanisms and depths differ between S0173a and S0235b.

292 Besides free-surface reflections, source-side scattering also includes another depth phase that reflects from Layer  
293 1 (underside reflection) at the source side. The arrival and polarity of this underside reflection depend on the focal  
294 depth and focal mechanism. This phase may be present between the direct SH wave and the SH-wave reflection. For  
295 example, we find a signal at about 5 seconds after the direct SH arrival for events S1048d, S0173a, and S0809a (Fig.  
296 2). We think it is likely to be the underside reflection at the source side for two reasons. First, the amplitudes of inter-  
297 layer reflections at the receiver side are much smaller (Fig. S5). Second, the polarity of this phase varies among  
298 different events (Fig. b1-e1), probably indicating its dependence on different focal mechanisms. Nevertheless, this  
299 positive signal (at about 5 s) does not interfere with the SH-wave reflection at around 10-11 s, and will not  
300 significantly influence our analysis. However, when source-side scattering (reflections off the free surface or Layer  
301 1) arrives at a similar time as the SH-wave reflection, it contaminates both the arrival time and the amplitude of the  
302 negative phase we are interested in. This might explain the amplitude discrepancies between the data and the synthetic  
303 SH-wave reflections for some events (e.g., S0173a, and S0809a in Fig. 4).

304 We note that, in our forward modeling of the synthetic waveforms with planar SH-wave incidence, only receiver-  
305 side scattering (e.g., SH-wave reflections and their multiples) is calculated, and source-side scattering is excluded  
306 (e.g., depth phases). We specifically chose this computational method because we have very little information on the  
307 focal depths and source-side structure. To benchmark our computations, we also calculated the synthetic waveforms  
308 using another orthonormal propagator algorithm, QSEIS (Wang, 1999), for events at various depths (from 15 km to  
309 50 km with an interval of 5 km) and then stacked all the QSEIS-synthetics. We found that the SH-wave reflection in  
310 the stacked waveform is very similar to the one calculated with planar wave incidence (Fig. S6a). Therefore, the  
311 planar S-wave incidence technique used here is reliable, especially since our analysis is based on the stacked cross-

312 correlation maps from five different events.

## 313 3.2 Uncertainties

314 Various factors can contribute to model uncertainties. For instance, glitches, if present in the time window of the  
315 S-wave reflections, will affect our analysis and results. Thus, to fully understand their possible influence, we analyzed  
316 both the raw data and deglitched data (Fig. S7). We found that none of the nine events used show any glitch within  
317 the selected time window (from -18 to 18 s). Glitches, therefore, do not affect the results presented here.

318 Source parameters (e.g., focal depths and focal mechanism) influence the arrival time and amplitude of the entire  
319 wave train. However, they likely do not strongly influence our results because they have a similar impact on both the  
320 direct phase and the receiver-side reflections due to their almost identical take-off angles and identical ray paths away  
321 from the receiver.

322 For similar reasons, attenuation in the deeper crust and mantle will affect the direct phase and reflections in the  
323 same way. Therefore, mantle attenuation only slightly influences our results when we normalize the trace to the direct  
324 phase. Only the attenuation in Layer 1 will influence them differently. However, due to the very short propagation  
325 distance within Layer 1, even a highly-attenuating model (e.g., with  $Q_s$  equals 150) does not change the reflected  
326 phases significantly (Fig. S6b). The same holds for the influence of possible errors in the mantle model.

327 There are also uncertainties (less than 5 degrees) in the epicentral distance of the quality-A marsquakes we utilized  
328 due to the uncertainties in the P- and S-phase picking (Clinton et al., 2021; InSight Marsquake Service, 2020, 2021a,  
329 b, 2022a, b) and in the Mars 1-D model. Inaccurate epicentral distance will result in a deviated ray parameter, and  
330 this error will propagate into the cross-correlation map, although the influence is subtle within the uncertainty range  
331 (Fig. S8). To take this source of uncertainty into account, we chose the minimum and maximum epicentral distances

332 (Clinton et al., 2021; InSight Marsquake Service, 2020, 2021a, b, 2022a, b) to calculate two synthetic waveforms and  
333 then derived two cross-correlation maps for each event. Our final cross-correlation map (Fig. 3a) results from the  
334 summation of the cross-correlation maps of these two end-member epicentral distances (Fig. S8) and therefore  
335 includes the propagation of uncertainties in the epicentral distance.

336 There are also uncertainties in the estimated back azimuth, which will influence the SH waveforms on the  
337 tangential component (during the rotation from North-East to Radial-Tangential components). We tested that, given  
338 the uncertainties in the back azimuth (Clinton et al., 2021; InSight Marsquake Service, 2020, 2021a, b, 2022a, b), the  
339 SH-waveform only slightly changes and the arrival time is almost constant (Fig. S1).

### 340 3.3 Interface Sharpness

341 Both our results and those from the RF study assume a sharp interface. If this is the case, since the SH-wave  
342 reflection and the RF are sampling the same discontinuity at the same depth, the observed  $V_{SH} < V_{SV}$  implies  
343 anisotropy within Layer 1. If the interface of Layer 1 is gradual (e.g., with a thickness of 2 km), synthetic inversion  
344 tests in which we assumed a sharp interface during the inversion show that the RF still samples the mid-point of this  
345 gradual interface (Fig. S9a). However, in this case, the inverted depth from the SH-wave reflection is shallower than  
346 the mid-point of the gradual interface. This result is consistent with the larger time shift of the SH-wave reflection  
347 (Fig. S9b) compared with the almost invisible change of the arrival for the P- to s-wave RF (Fig. S9c). This means  
348 that, if the interface is gradual, SH-wave reflection underestimates the depth of Layer 1 compared with RFs. Therefore,  
349 the reflection-derived region ( $V_{SH}$ ) would shift to larger depths (Fig. 5b, c), which implies an even greater difference  
350 between  $V_{SH}$  and  $V_{SV}$ . Thus, whether the interface of Layer 1 is sharp or gradual, the evidence of  $V_{SH} < V_{SV}$  is robust.

### 351 3.4 Dipping and Curved Interface

352 An alternative to the proposed radial anisotropy to explain the discrepancies between the RF- and reflection-derived

353  $V_S$  models is the existence of a dipping and curved interface because the point where the incident wave enters Layer  
354 1 differs between the SH-wave reflections (Fig. S10a) and the P-wave RFs (Fig. S10b).

355 Based on ray theory, the horizontal distance between the InSight lander and the point where SH-waves enter Layer  
356 1 is between 1.9 km and 4.2 km. Additionally, the RF samples a region closer to the lander site (Fig. S10b). If we  
357 assume that Layer 1 is shallower beneath the lander site, even if it is isotropic ( $V_{SH} = V_{SV}$ , see Fig. S10c and S10d),  
358 models constrained from SH-wave reflections also yield later arrival times (i.e., 10-11 s, shown in Fig. 2) than the  
359 RFs-derived models (i.e., 9 s, Fig. 4) since SH-wave reflections are sampling regions farther away from the receiver.

360 Nevertheless, given the size of the S-wave Fresnel zone (about 3 – 8 km) and the shorter distance (< 4.2 km)  
361 between the lander and the point where S-waves enter Layer 1, dipping layer or small-scale topography (e.g., curved  
362 interface) may have limited influence on the results.

### 363 3.5 Seismic Anisotropy

364 The average radial anisotropy coefficient,  $\xi = (V_{SH}/V_{SV})^2$ , in Layer 1 (at  $8 \pm 2$  km depth) of the martian crust  
365 ranges from 0.7 to 0.9. Similar radial anisotropy observations have been reported in various regions on Earth. For  
366 example, a  $\xi$  value of 0.8 has been found in the upper crust (top 5 km) in Iceland (Volk et al., 2021), and lower SH-  
367 wave speeds by at least -12% compared with SV-waves have been observed in the middle crust (5 – 20 km) of  
368 southern Madagascar (Dreiling et al., 2018). Another SH-wave speed reduction of -5% has been identified in the top  
369 8 km of the crust in the eastern part of the Variscan orogeny (Acevedo et al., 2021).

370 The amplitude ( $\xi < 1$ ) of the detected anisotropy may be the seismic signature of vertical dry or gas-filled fractures  
371 due to the extension of impact-related stresses, normal faults due to crustal extension, or vertical liquid intrusions  
372 such as melt pockets, magmatic dykes, and water-saturated fractures (Bastow et al., 2010; Dreiling et al., 2018; Volk  
373 et al., 2021). We prefer to consider water-saturated (rather than ice-filled) fractures because Manga and Wright (2021)

374 found that there is no cryosphere beneath the InSight lander site since the S-wave speed from the RF study  
375 (Knapmeyer-Endrun et al., 2021) is too low to be ice-saturated.

376 On Mars, the study of Knapmeyer-Endrun et al. (2021) suggests an upper crust with very low density for the top  
377 10 km ( $< 2000 \text{ kg/m}^3$ , constrained from RF waveforms data), increasing at depths greater than 10 km to values close  
378 to those ( $\sim 2600 \text{ kg/m}^3$ ) proposed by Goossens et al. (2017) based on orbital gravity data. Such a low density, if  
379 confirmed, could indicate the presence of less dense sedimentary rocks (Pan et al., 2020) and/or rocks with porosity  
380 in Layer 1 (e.g., Lognonné et al., 2020; Knapmeyer-Endrun et al., 2021). Increased porosity is compatible with large  
381 impact (e.g., Johnson et al. 2021) and associated fractures or pore space as possible candidates that could generate  
382 the observed radial anisotropy. These effects can furthermore be amplified near the equator and in the vicinity of the  
383 InSight landing site, where ground ice is not stable (e.g., Clifford et al., 2010), which will lead ultimately to large,  
384 gas-filled cracks and connected porosity.

385 In addition to radial anisotropy, which quantifies the difference in wave speed between the vertical and horizontal  
386 direction, a medium can be azimuthally anisotropic, in which case the wave speed varies with the azimuth of  
387 propagation. Constraining both types of anisotropy is essential to obtain a more complete description of the elastic  
388 properties of the planet interior. With the current approach, which compares SV- and SH-wave speeds from RF and  
389 SH-reflection analysis to infer seismic anisotropy, a range of back azimuths is required to constrain azimuthal  
390 anisotropy. However, all the quality-A marsquakes with known back azimuth occurred roughly to the east of the  
391 lander, making a robust estimate of azimuthal anisotropy impossible at this point.

392 Shear-wave splitting with a single measurement could provide insights into azimuthal anisotropy (e.g., Silver and  
393 Chan, 1988). However, waveform distortions, probably due to the near- or post-critical reflection at the surface (e.g.,  
394 Savage, 1999), prevent us from measuring shear-wave splitting with traditional methods (see Fig. S11 and S12, and  
395 discussion can be found in the supplementary material).

## 396 3.6 Anisotropy Modeling

397 To model the observed radial anisotropy, without loss of generality, we consider a situation of preferred alignment  
398 of intrusions, which can represent various situations (e.g., intrusions of gas- or liquid-filled space, or melt pockets  
399 with different physical parameters). The model setup is shown in Fig. 7a: an isotropic background matrix ( $V_P = 2.8$   
400 km/s,  $V_S = 1.4$  km/s) is reinforced with isotropic oblate spheroidal intrusions with a horizontal symmetry axis,  
401 resulting in a composite that is (horizontally) transversely isotropic. We used an analytical solution to determine the  
402 elasticity matrix of the effective medium (Tandon and Weng, 1984) and solved the Christoffel equation to determine  
403 quasi-SV and SH wave speeds (Walker and Wookey, 2012), from which we calculate  $\xi$ . We also tested other effective  
404 medium theories (e.g., Hudson, 1980), and found they give similar results.

405 For incoming S-waves with an incident angle of  $20^\circ$ , we modeled the variation of  $\xi$  as a function of four factors:  
406 the aspect ratio (minor axis over major axis) of the intrusion, the velocity contrast between the intrusion and the  
407 background matrix, the volume fraction of the intrusions, and the relationship between the orientation of the  
408 intrusions and the propagation azimuth of the incoming S-wave. Three example models are shown in Figure 7c,  
409 representing dry gas-filled ( $V_P = 0.24$  km/s,  $V_S = 0$  km/s, i.e., carbon dioxide) or water-filled ( $V_P = 1.5$  km/s,  $V_S = 0$   
410 km/s) cracks/fractures (i.e., intrusions with a significantly reduced seismic velocity), and intrusions with a faster  
411 seismic velocity ( $V_P = 6.3$  km/s,  $V_S = 3.4$  km/s, e.g., frozen igneous dikes with a larger wave speed than the porous  
412 rocks). All of these reproduce  $\xi$  values compatible with our observation, however, there are significant trade-offs  
413 between the input parameters. For example, Fig. 7d shows that the range of aspect ratios and volume fractions  
414 associated with low- and high-velocity intrusions can reproduce the observation: larger aspect ratio intrusions require  
415 significantly higher volume fractions to exhibit sufficient anisotropy. Furthermore, models incorporating seismically  
416 fast intrusions need considerably higher volume fractions to reproduce the data. For example, to exhibit similar  
417 anisotropy (in Fig. 7c), the volume fraction is required to be 0.5% and 10% for low- and high-velocity intrusions,

418 respectively.

419 A common feature of all the anisotropy models tested is that there is a strong dependence on the propagation  
420 azimuth of the incoming S-wave. For azimuths close to the strike direction of the intrusions, all the models show  $\xi < 1$ ,  
421 whereas for azimuths closer to perpendicular this switches to  $\xi > 1$ . In reality, for intermediate angles (at non-  
422 horizontal incidence) the two shear-waves are not strictly horizontally or vertically polarized and would more likely  
423 appear isotropic than the strongly discontinuous variation suggested by the curve. In other words, anisotropy of the  
424 kind modeled would not be readily apparent in the data at these azimuths. This is a limitation of the measurement  
425 approach rather than the modeling itself. Thus, it is clear that to reproduce the observed signal, the intrusions should  
426 be oriented approximately East-West, close to the sagittal plane of the marsquakes interpreted as originating from the  
427 East.

428 There are several plausible explanations for these models. Regional compressive stress in the crust is expected to  
429 preferentially close fractures quasi-normal to the direction of maximum compression (e.g., Kaneshima, 1990; Boness  
430 and Zoback, 2006). The region of western Elysium Planitia around the InSight location (Fig. 1a and 1b) shows  
431 evidence of approximately North-South trending ‘wrinkle ridges’ (Golombek et al, 2018; 2020). Wrinkle ridges result  
432 from the thrust faulting and folding of sub-regolith lava flows resulting from compressive stress, (e.g., Mueller and  
433 Golombek, 2004; Golombek and Phillips, 2010). This suggests an approximately East-West compression direction,  
434 which would preferentially close North-South trending fractures leaving East-West fractures open. Dry- or liquid-  
435 filled fractures representing a sufficient volume fraction could produce the observed anisotropy. The potential sources  
436 of regional stresses in the crust include lithospheric loading from the Elysium and Tharsis volcanic provinces  
437 (Banerdt et al, 1982; Hall et al, 1986) that might be modulated by global compression (e.g., Mangold et al, 2000;  
438 Golombek and Phillips, 2010; Ruj and Kawai, 2021).

439 A second possible mechanism to reproduce the observed anisotropy is allowed by the potential for high-velocity

440 intrusions in the crust. One explanation for such a model might be the presence of dike structures in the crust, from  
441 melting or volcanic events. Dike structures have been invoked as a mechanism for seismic anisotropy on Earth (e.g.,  
442 Snyder and Bruneton, 2007; Lee et al, 2021). Dike structures are associated with a range of geologic events including  
443 impact cratering; radial and concentric diking are observed around known impact craters on Earth (e.g., Lambert,  
444 1981; Head and Mustard, 2006) formed by impact melting. The InSight lander is on the western edge of a large (~175  
445 km diameter, see Fig. 1b) quasi-circular depression, interpreted as a degraded, buried impact crater of approximately  
446 Noachian age (Golombek et al, 2018). Radial dikes associated with this crater would have an approximately East-  
447 West orientation beneath InSight, providing a second possible contributing mechanism to the observed anisotropy.  
448 Such a mechanism also provides an additional explanation for extensive faulting and fracturing in the crust below  
449 InSight.

450 A joint inversion with the constraints from density studies (e.g., Baratoux et al., 2014; Knapmeyer-Endrun et al.,  
451 2021) could help better determine the aspect ratio, wave speed, and volume fraction of the intrusions in the future,  
452 potentially enabling us to distinguish between these mechanisms.

453

454

455

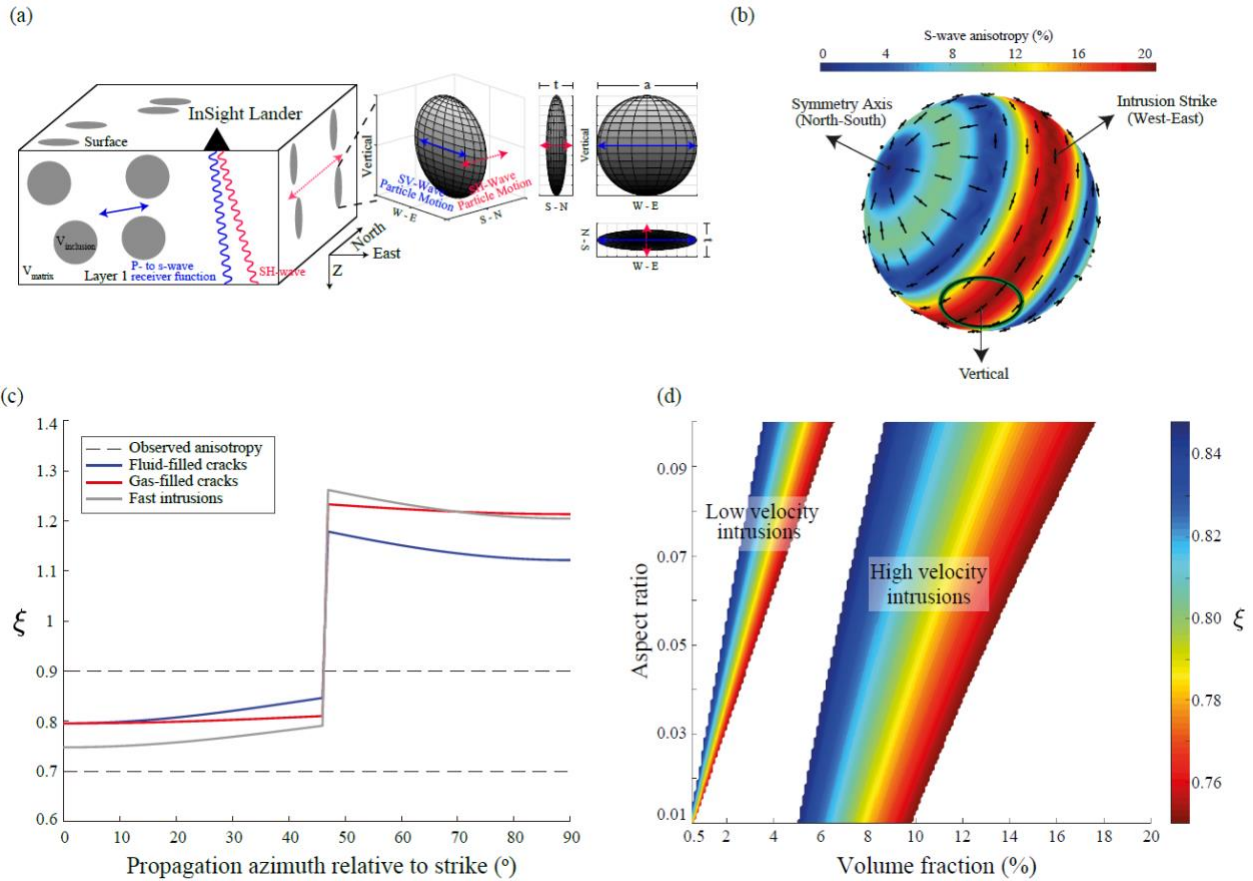


Figure 7. Proposed mechanism for the measured anisotropy in Layer 1 at the InSight lander site.

- (a) The left panel shows an isotropic background matrix including isotropic disk-like inclusions (in grey). The black triangle represents the InSight lander, and the blue and red lines mark the incoming ray paths for the P- to s-wave receiver function and SH-wave reflection, respectively. The blue and red arrows denote their polarization directions (SV-wave in the Z-E plane, and SH-wave along the N-S direction). The composite is transversely anisotropic with a symmetry axis along the N-S direction. The right panels present details on the ellipsoidal inclusion, where  $t$  and  $a$  are the minor and major axes.
- (b) S-wave anisotropy and orientation of fast shear-wave for an example model of low-velocity (liquid) inclusions following theory of Tandon and Weng (1984). The green circle denotes the range of wave propagation azimuths modelled, with an incident angle of  $20^\circ$ . Color scale indicates difference between fast and slow shear-wave velocities.
- (c) Radial anisotropy coefficient,  $\xi = (V_{SH}/V_{SV})^2$ , for three example models representing fractures (liquid- or gas-filled, blue and red curves, respectively), and high velocity (e.g., igneous) intrusions (grey curve) with constraints from observation (grey dashed lines). All models have aspect ratios of 0.01, and volume fractions of 0.5% (low velocity intrusions) and 10% (high velocity).
- (d) Trade-off between parameters adopted in models. The color scale shows the modelled  $\xi$  as a function of the inclusion aspect ratio and volume fraction.

## 467 **Conclusions**

468 We have made the first detection of SH-wave reflections on the tangential component for broadband and low-  
469 frequency marsquakes (quality-A) with epicentral distances smaller than 60 degrees, which helps us constrain the  
470 crust at the lander site. Specifically, we found coherent signals from five events that appear to be independent of the  
471 focal depth and are consistent with SH-wave reflections off the first crustal interface (Layer 1). This phase confirms  
472 the existence of the  $\sim 8$  km interface in the crust and the large wave speed (or impedance) contrast across it.

473 The range of acceptable parameters determined from the analysis of SH-waves does not intersect with the majority  
474 of the models from a previous RF study, which constrains the speed of SV waves (Knapmeyer-Endrun et al., 2021).  
475 We propose that this inconsistency results from the presence of seismic anisotropy within the top crustal layer at the  
476 lander site. Modeling results show that dry or liquid-filled cracks/fractures, and igneous intrusions can reproduce the  
477 observed radial anisotropy ( $V_{SH} < V_{SV}$ ). A joint inversion with the constraints from density studies could help better  
478 determine the aspect ratio, wave speed, and volume fraction of the intrusions in the future, potentially enabling us to  
479 distinguish between these mechanisms. More high-quality marsquakes with a larger range of back-azimuth variation  
480 would help further study the azimuthal anisotropy and better constrain the elastic properties of the Martian crust.

## 482 **Acknowledgments**

483 J.L. thanks Tong Zhou (from the InSightSeers program) for assistance in the anisotropy modeling and benchmarks  
484 for the synthetic waveforms calculation. J.L. thanks Ross Maguire for providing the Marsquakes downloading script  
485 (InSight SEIS Data Bundle, 2021). We thank reviewer Martha Savage and another anonymous reviewer for their

486 helpful reviews.

487 J.L. and C.B. were supported by NASA InSight PSP grant #80NSSC18K1679. J.W was supported by a UKSA  
488 Aurora Grant (ST/T002972/1). P.L, E.S., and J.P.M. are supported by ANR MAGIS (ANR-19-CE31-0008-08) and  
489 by CNES for SEIS science support. M.S. thanks SANIMS (RTI2018-095594-B-I00).

490 This is InSight Contribution Number 237. InSight seismic data presented here  
491 ([http://dx.doi.org/10.18715/SEIS.INSIGHT.XB\\_2016](http://dx.doi.org/10.18715/SEIS.INSIGHT.XB_2016)) is publicly available through the Planetary Data System (PDS)  
492 Geosciences node, the Incorporated Research Institutions for Seismology (IRIS) Data Management Center under  
493 network code XB, and through the data center of Institut de Physique du Globe, Paris (<http://seis-insight.eu>). We  
494 acknowledge NASA, CNES, their partner agencies and Institutions (UKSA, SSO, DLR, JPL, IPGP-CNRS, ETHZ,  
495 IC, MPS-MPG) and the flight operations team at JPL, SISMOC, MSDS, IRIS-DMC and PDS for providing SEED  
496 SEIS data. A portion of the work was supported by the InSight Project at the Jet Propulsion Laboratory, California  
497 Institute of Technology, under a contract with the National Aeronautics and Space Administration.

498

499

500

501

502

## References

- 504 1. Acevedo, J., Fernández-Viejo, G., Llana-Fúnez, S., López-Fernández, C., Olona, J., & Pérez-  
505 Millán, D. (2022). Radial anisotropy and S-wave velocity depict the internal to external zone  
506 transition within the Variscan orogen (NW Iberia). *Solid Earth*, 13(3), 659-679.
- 507 2. Banerdt, W., Phillips, R., Sleep, N., & Saunders, R., 1982. Thick shell tectonics on one-plate  
508 planets: Applications to Mars, *Journal of Geophysical Research: Solid Earth*, 87(B12), 9723–  
509 9733.
- 510 3. Banerdt, W.B., Smrekar, S.E., Banfield, D., Giardini, D., Golombek, M., Johnson, C.L.,  
511 Lognonné, P., Spiga, A., Spohn, T., Perrin, C. and Stähler, S.C., 2020. Initial results from the  
512 InSight mission on Mars. *Nature Geoscience*, 13(3), pp.183-189.
- 513 4. Baratoux, D., Samuel, H., Michaut, C., Toplis, M. J., Monnereau, M., Wieczorek, M., Garcia, R.,  
514 & Kurita, K., 2014. Petrological constraints on the density of the martian crust, *Journal of*  
515 *Geophysical Research: Planets*, 119(7), 1707–1727.
- 516 5. Bastow, I., Pilidou, S., Kendall, J.-M., & Stuart, G., 2010. Melt-induced seismic anisotropy and  
517 magma assisted rifting in Ethiopia: Evidence from surface waves, *Geochemistry, Geophysics,*  
518 *Geosystems*, 11(6).
- 519 6. Boness, N. L. & Zoback, M. D., 2006. Mapping stress and structurally controlled crustal shear  
520 velocity anisotropy in California, *Geology*, 34(10), 825–828.
- 521 7. Brinkman, N., Stähler, S. C., Giardini, D., Schmelzbach, C., Khan, A., Jacob, A., Fuji, N., Perrin,  
522 C., Lognonné, P., Beucler, E., et al., 2021. First focal mechanisms of marsquakes, *Journal of*  
523 *Geophysical Research: Planets*, 126(4), e2020JE006546.
- 524 8. Ceylan, S., Clinton, J., Giardini, D., Boese, M., Charalambous, C., van Driel, M., Horleston, A.,  
525 Kawamura, T., Khan, A., Orhand-Mainsant, G. and Scholz, J.R., 2020. Companion guide to the  
526 Marsquake Catalog from InSight, Sols 0-478: data content and non-seismic events, *Physics of the*  
527 *Earth and Planetary Interiors*, 310, 106597.
- 528 9. Clinton, J. F., Ceylan, S., van Driel, M., Giardini, D., Stähler, S. C., Böse, M., Charalambous, C.,  
529 Dahmen, N. L., Horleston, A., Kawamura, T., et al., 2021. The marsquake catalogue from  
530 InSight, sols 0–478, *Physics of the Earth and Planetary Interiors*, 310, 106595.
- 531 10. Clifford, S.M., Lasue, J., Heggy, E., Boisson, J., McGovern, P. and Max, M.D., 2010. Depth of  
532 the Martian cryosphere: Revised estimates and implications for the existence and detection of  
533 subpermafrost groundwater. *Journal of Geophysical Research: Planets*, 115(E7).
- 534 11. Compaire, N., Margerin, L., Garcia, R. F., Pinot, B., Calvet, M., Orhand-  
535 Mainsant, G., Kim, D., Lekic, V., Tauzin, B., Schimmel, M., et al., 2021. Autocorrelation of  
536 the ground vibrations recorded by the seis-insight seismometer on mars, *Journal of Geophysical*  
537 *Research: Planets*, 126(4), e2020JE006498.
- 538 12. Dreiling, J., Tilmann, F., Yuan, X., Giese, J., Rindraharisaona, E. J., Rumpker, G., &  
539 Wyssession, M. E., 2018. Crustal radial anisotropy and linkage to geodynamic processes: a study  
540 based on seismic ambient noise in southern Madagascar, *Journal of Geophysical Research: Solid*  
541 *Earth*, 123(6), 5130– 5146.
- 542 13. Edwards, C.S., Nowicki, K.J., Christensen, P.R., Hill, J., Gorelick, N. and Murray, K., 2011.  
543 Mosaicking of global planetary image datasets: 1. Techniques and data processing for Thermal

- 544 Emission Imaging System (THEMIS) multi-spectral data. *Journal of Geophysical Research:*  
545 *Planets*, 116(E10).
- 546 14. Giardini, D., Lognonné, P., Banerdt, W. B., Pike, W. T., Christensen, U., Ceylan, S., Clinton, J. F.,  
547 van Driel, M., Stähler, S. C., Böse, M., et al., 2020. The seismicity of Mars, *Nature Geoscience*,  
548 13(3), 205 – 212.
- 549 15. Goossens, S., Sabaka, T.J., Genova, A., Mazarico, E., Nicholas, J.B. and Neumann, G.A., 2017.  
550 Evidence for a low bulk crustal density for Mars from gravity and topography. *Geophysical*  
551 *research letters*, 44(15), pp.7686-7694.
- 552 16. Golombek, M.P., and Phillips, R.J., Mars tectonics, in *Planetary Tectonics*, ed. by T.R. Watters,  
553 R.A. Schultz (Cambridge University Press, Cambridge, 2010), pp. 183–232. Chap. 5
- 554 17. Golombek, M., Grott, M., Kargl, G., Andrade, J., Marshall, J., Warner, N., Teanby, N. A., Ansan,  
555 V., Hauber, E., Voigt, J., et al., 2018. Geology and physical properties investigations by the  
556 InSight lander, *Space Science Reviews*, 214(5), 1–52.
- 557 18. Golombek, M., Warner, N., Grant, J., Hauber, E., Ansan, V., Weitz, C., Williams, N.,  
558 Charalambous, C., Wilson, S., DeMott, A., et al., 2020. Geology of the insight landing site on  
559 mars, *Nature communications*, 11(1), 1–11.
- 560 19. Hall, J. L., Solomon, S. C., & Head, J. W., 1986. Elysium region, mars: Tests of lithospheric  
561 loading models for the formation of tectonic features, *Journal of Geophysical Research: Solid*  
562 *Earth*, 91(B11), 11377–11392.
- 563 20. Hauck, S.A. and Phillips, R.J., 2002. Thermal and crustal evolution of Mars. *Journal of*  
564 *Geophysical Research: Planets*, 107(E7), pp.6-1.
- 565 21. Head, J. W. & Mustard, J. F., 2006. Breccia dikes and crater-related faults in impact craters on  
566 mars: Erosion and exposure on the floor of a crater 75 km in diameter at the dichotomy boundary,  
567 *Meteoritics & Planetary Science*, 41(10), 1675–1690.
- 568 22. Hudson, J. A., 1981. Wave speeds and attenuation of elastic waves in material containing cracks,  
569 *Geophysical Journal International*, 64(1), 133–150.
- 570 23. InSight Marsquake Service, 2019-2022. Mars Seismic Catalogue, InSight Mission; V1, V7, V8,  
571 V9, V10.
- 572 24. InSight Mars SEIS Data Service. 2019. SEIS raw data, Insight Mission. IPGP, JPL, CNES,  
573 ETHZ, ICL, MPS, ISAE-Supaero, LPG, MFSC.
- 574 25. InSight SEIS Data Bundle. 2021. PDS Geosciences (GEO) Node.
- 575 26. Johnson, B.C., Milliken, R.E., Lewis, K.W. and Collins, G.S., 2021. Impact generated porosity in  
576 Gale crater and implications for the density of sedimentary rocks in lower Aeolis  
577 Mons. *Icarus*, 366, p.114539.
- 578 27. Kaneshima, S., 1990. Origin of crustal anisotropy: Shear wave splitting studies in Japan, *Journal*  
579 *of Geophysical Research: Solid Earth*, 95(B7), 11121–11133.
- 580 28. Kennett, B.L.N., 2009. *Seismic wave propagation in stratified media*, ANU Press.
- 581 29. Knapmeyer-Endrun, B., Panning, M. P., Bissig, F., Joshi, R., Khan, A., Kim, D., Lekic, V.,  
582 Tauzin, B., Tharimena, S., Plasman, M., et al., 2021. Thickness and structure of the martian crust  
583 from InSight seismic data, *Science*, 373(6553), 438 – 443.
- 584 30. Lambert P. 1981. Breccia dikes—Geological constraints on the formation of complex craters. In  
585 *Multi-ring basins: Formation and evolution*. New York: Pergamon Press. pp. 59 – 78.
- 586 31. Langston, C. A., 1979. Structure under Mount Rainier, Washington, inferred from teleseismic  
587 body waves, *Journal of Geophysical Research: Solid Earth*, 84(B9), 4749–4762.

- 588 32. Lee, S.-J., Kim, S., Rhie, J., Kang, T.-S., & Kim, Y., 2021. Upper crustal shear wave velocity and  
589 radial anisotropy beneath Jeju island volcanoes from ambient noise tomography, *Geophysical*  
590 *Journal International*, 225(2), 1332–1348.
- 591 33. Liu, T. & Shearer, P. M., 2021. Complicated lithospheric structure beneath the contiguous US  
592 revealed by teleseismic reflections, *Journal of Geophysical Research: Solid Earth*, 126(5),  
593 e2020JB021624.
- 594 34. Lognonné, P., Banerdt, W.B., Giardini, D., Pike, W.T., Christensen, U., Laudet, P., De Raucourt,  
595 S., Zweifel, P., Calcutt, S., Bierwirth, M. and Hurst, K.J., 2019. SEIS: Insight’s seismic  
596 experiment for internal structure of Mars. *Space Science Reviews*, 215(1).
- 597 35. Lognonné, P., Banerdt, W., Pike, W., Giardini, D., Christensen, U., Garcia, R. F., Kawamura, T.,  
598 Kedar, S., Knapmeyer-Endrun, B., Margerin, L., et al., 2020. Constraints on the shallow elastic  
599 and anelastic structure of Mars from InSight seismic data, *Nature Geoscience*, 13(3), 213–220.
- 600 36. Mangold, N., Allemand, P., Thomas, P., & Vidal, G., 2000. Chronology of compressional  
601 deformation on mars: Evidence for a single and global origin, *Planetary and Space Science*,  
602 48(12-14), 1201–1211.
- 603 37. Mueller, K. & Golombek, M., 2004. Compressional structures on mars, *Annu. Rev. Earth Planet.*  
604 *Sci.*, 32, 435–464.
- 605 38. Pan, L. et al. Crust stratigraphy and heterogeneities of the first kilometers at the dichotomy  
606 boundary in western Elysium Planitia and implications for InSight lander. *Icarus* 338, 113511  
607 (2020).
- 608 39. Plesa, A.-C., Padovan, S., Tosi, N., Breuer, D., Grott, M., Wieczorek, M., Spohn, T., Smrekar, S.,  
609 & Banerdt, W., 2018. The thermal state and interior structure of Mars, *Geophysical Research*  
610 *Letters*, 45(22), 12–198.
- 611 40. Ruj, T., and Kawai, K., 2021, A global investigation of wrinkle ridge formation events;  
612 Implications towards the thermal evolution of Mars, *Icarus* 369 (2021) 114625
- 613 41. Savage, M.K., 1999. Seismic anisotropy and mantle deformation: what have we learned from  
614 shear wave splitting?. *Reviews of Geophysics*, 37(1), pp.65-106.
- 615 42. Schimmel, M., Stutzmann, E., Lognonné, P., Compaire, N., Davis, P., Drilleau, M., Garcia, R.,  
616 Kim, D., Knapmeyer-Endrun, B., Lekic, V., et al., 2021. Seismic noise autocorrelations on mars,  
617 *Earth and Space Science*, p. e2021EA001755.
- 618 43. Scholz, J.-R., Widmer-Schmidrig, R., Davis, P., Lognonné, P., Pinot, B., Garcia, R. F., Hurst, K.,  
619 Pou, L., Nimmo, F., Barkaoui, S., et al., 2020. Detection, analysis, and removal of glitches from  
620 InSight’s seismic data from Mars, *Earth and Space Science*, 7(11), e2020EA001317.
- 621 44. Shearer, P. M., 2019. Introduction to seismology, Cambridge University press.
- 622 45. Shearer, P. M. & Buehler, J., 2019. Imaging upper-mantle structure under USarray using long-  
623 period reflection seismology, *Journal of Geophysical Research: Solid Earth*, 124(9), 9638–9652.
- 624 46. Silver, P. G., & Chan, W. W. (1988). Implications for continental structure and evolution from  
625 seismic anisotropy. *Nature*, 335(6185), 34-39.
- 626 47. Smith, D.E., Zuber, M.T., Frey, H.V., Garvin, J.B., Head, J.W., Muhleman, D.O., Pettengill, G.H.,  
627 Phillips, R.J., Solomon, S.C., Zwally, H.J. and Banerdt, W.B., 2001. Mars Orbiter Laser  
628 Altimeter: Experiment summary after the first year of global mapping of Mars. *Journal of*  
629 *Geophysical Research: Planets*, 106(E10), pp.23689-23722.
- 630 48. Snyder, D. & Bruneton, M., 2007. Seismic anisotropy of the slave craton, NW Canada, from joint  
631 interpretation of SKS and Rayleigh waves, *Geophysical Journal International*, 169(1), 170–188.

- 632 49. Stähler, S. C., Khan, A., Banerdt, W. B., Lognonné, P., Giardini, D., Ceylan, S., Drilleau, M.,  
633 Duran, A. C., Garcia, R. F., Huang, Q., et al., 2021. Seismic detection of the martian core,  
634 Science, 373(6553), 443–448.
- 635 50. Tandon, G. P. & Weng, G. J., 1984. The effect of aspect ratio of intrusions on the elastic  
636 properties of unidirectionally aligned composites, Polymer composites, 5(4), 327–333.
- 637 51. Volk, O., White, R. S., Pilia, S., Green, R. G., Maclennan, J., & Rawlinson, N., 2021. Oceanic  
638 crustal flow in Iceland observed using seismic anisotropy, Nature Geoscience, 14(3), 168–173.
- 639 52. Wang, R., 1999. A simple orthonormalization method for stable and efficient computation of  
640 Green’s functions, Bulletin of the Seismological Society of America, 89(3), 733–741.

641

642

643

644

645

646

647

648

649

## 650 **Supplementary Material**

### 651 **Summary**

652 There are 12 figures and 1 table in this supplementary material. We also discussed azimuthal anisotropy and shear-  
653 wave splitting in this supplementary material.

654 **Azimuthal anisotropy and shear-wave splitting**

655 Shear-wave splitting with a single measurement could provide insights into azimuthal anisotropy (e.g., Silver and  
656 Chan, 1988). The anisotropy modeling results (Fig. 7b) indicate that the East-West (E-W) direction is the fast azimuth.  
657 Therefore, for the shear-wave splitting, we should expect earlier arrivals on the E-W components than the N-S  
658 components.

659 We examined the shear-wave splitting of the direct S-waves for the five events used in our study (Fig. S11). For  
660 events S1048d and S1133c, there is no strong energy on the N-S component, probably due to the polarization  
661 directions (which depend on the focal mechanism) of the S-wave. For the other three events (S0235b, S0173a, and  
662 S0809a), the waveforms on the N-S and E-W components are not similar, which hinders the splitting measurements.  
663 Despite the lack of similarity, the waveforms on the E-W component seem to show delayed, rather than earlier,  
664 arrivals than those on the N-S component.

665 However, we found that this seeming contradiction is likely caused by the distortion of the waveforms. On Earth,  
666 when the incidence angle is larger than the surface wave window (e.g.,  $35^\circ$ ), the SsPmp phase (generated at the Moho  
667 with a near- or post-critical reflection at the surface) distorts both the phase and amplitude of the SV-waveforms  
668 (Savage, 1999). We found that this distortion is more likely to occur on Mars since Layer 1 is located at a shallower  
669 depth (i.e.,  $\sim 8$  km) than the average Moho on Earth. Synthetic waveforms on the E-W component, using an isotropy  
670 model (Layer 1 at 8 km) show that the arrivals of the S-to-p conversion (at Layer 1) and the SsPp phase (generated  
671 at Layer 1, with a near- or post-critical S-to-P reflection at the free surface) are -2 s and 4.5 s, respectively (Fig. S12a,  
672 the Gaussian width of the source time function is  $\sim 0.38$  s). When the duration of the source time function increases  
673 (Fig. S12b-d), those two phases overlap with the direct SV-phase. Therefore, the shape of the SV-waveforms on the  
674 E-W component is no longer similar to that of the SH-waveforms on the N-S component. In addition, for this isotropic  
675 model, the waveforms on the E-W component seem to arrive earlier than those on the N-S component, which is

676 similar to what we have observed for the three marsquakes (S0235b, S0173a, and S0809a).

677 Therefore, on Mars, we cannot directly measure the shear-wave splitting with the currently available events due to

678 the presence of those two phases generated from Layer 1 on the N-S component.

679

680

## 681 References

682 1. Silver, P. G., & Chan, W. W. (1988). Implications for continental structure and evolution from  
683 seismic anisotropy. *Nature*, 335(6185), 34-39.

684 2. Savage, M.K., 1999. Seismic anisotropy and mantle deformation: what have we learned from  
685 shear wave splitting?. *Reviews of Geophysics*, 37(1), pp.65-106.

686

687

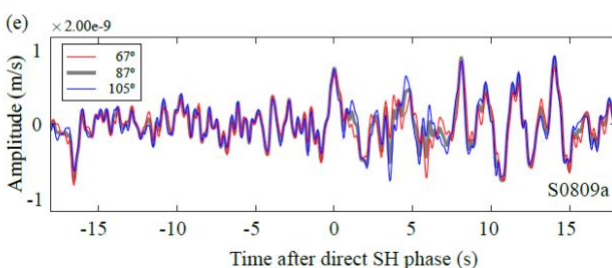
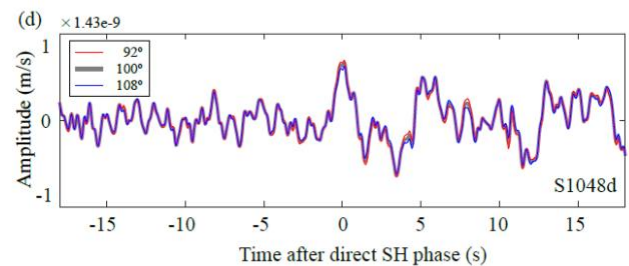
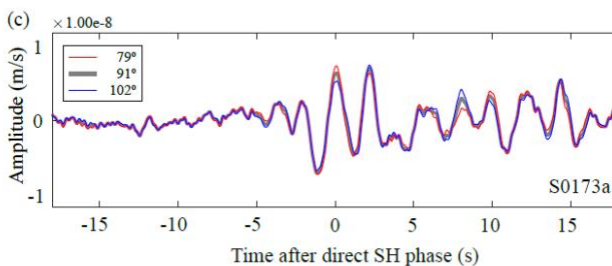
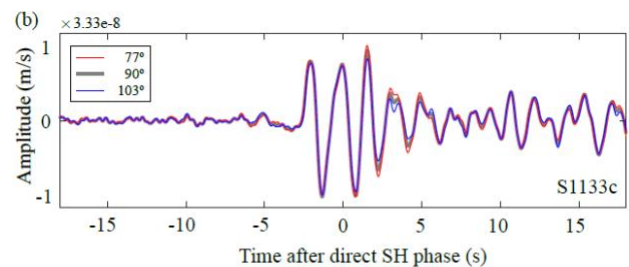
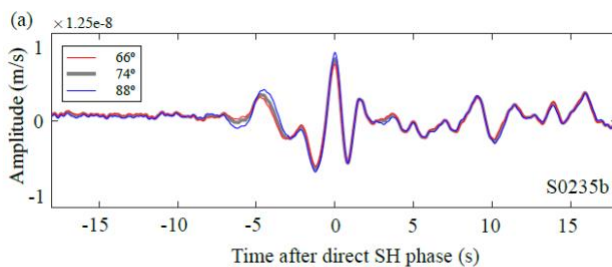
688

689

690

691

692



693

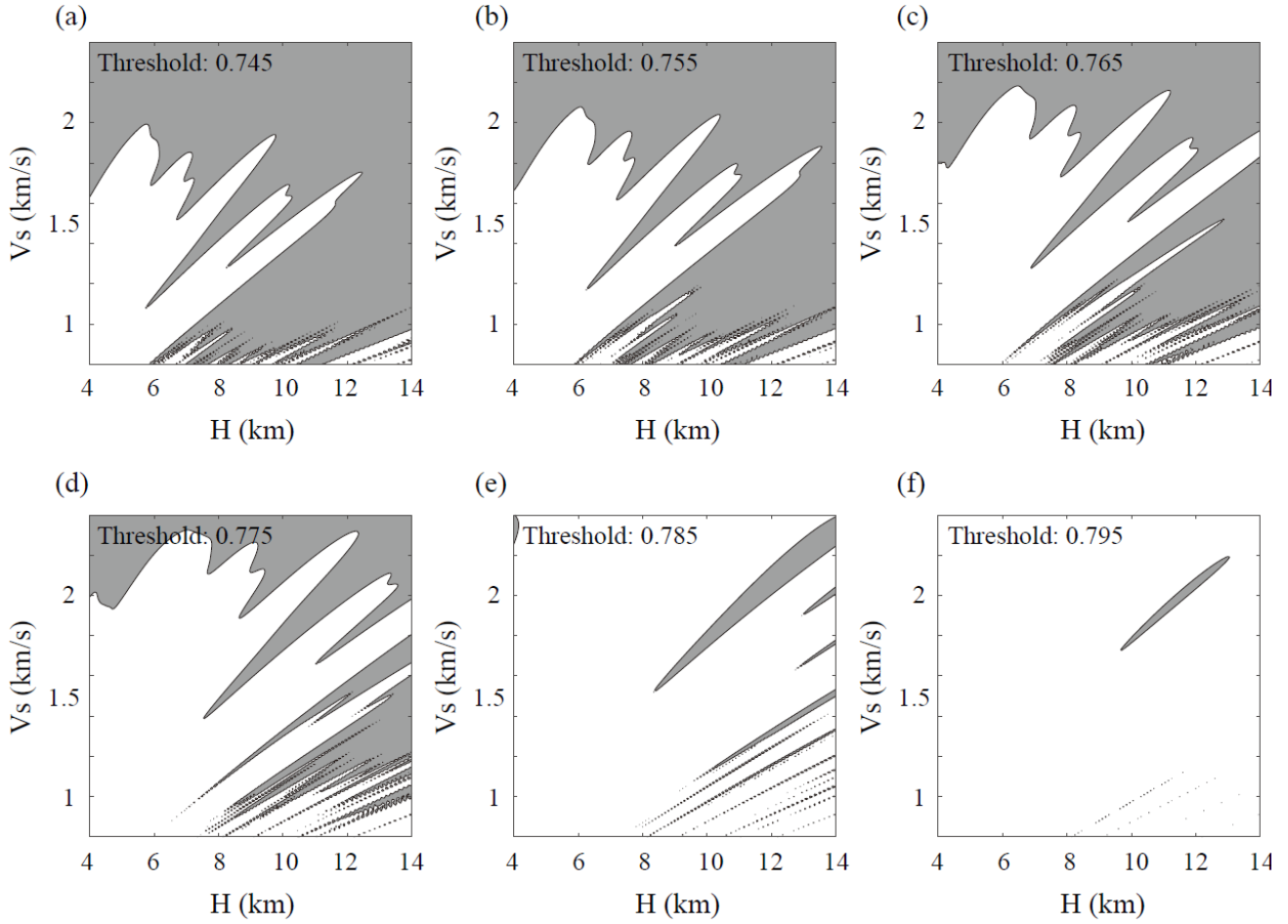
694

695 **Figure S1.** Influence of the back-azimuth uncertainties on the SH-wave reflections for events (a) S0235b, (b) 1133c,  
696 (c) S0173a, (d) 1048d, and (e) S0809a. Velocity waveforms are shown on the tangential component. The red, grey  
697 and blue colors correspond to different back azimuths as noted in the legend of each panel.

698

699

700



701

702 **Figure S2.** Model constraints from the SH-wave reflections with different thresholds.

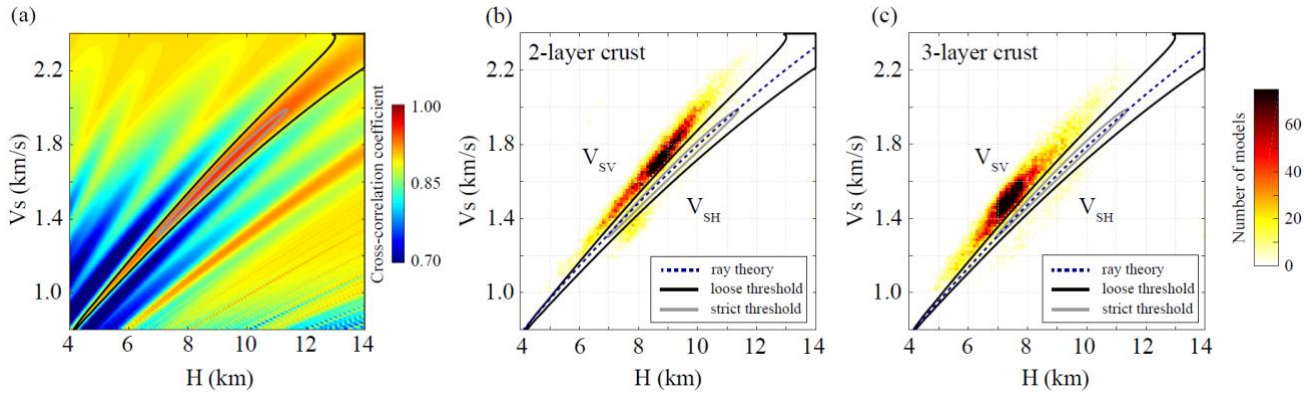
703 (a) Acceptable model region (in grey), derived from Fig. 5a, with a threshold of 0.745.

704 Similar analysis for threshold of (b) 0.755, (c) 0.765, (d) 0.775, (e) 0.785, and (f) 0.795.

705

706

707



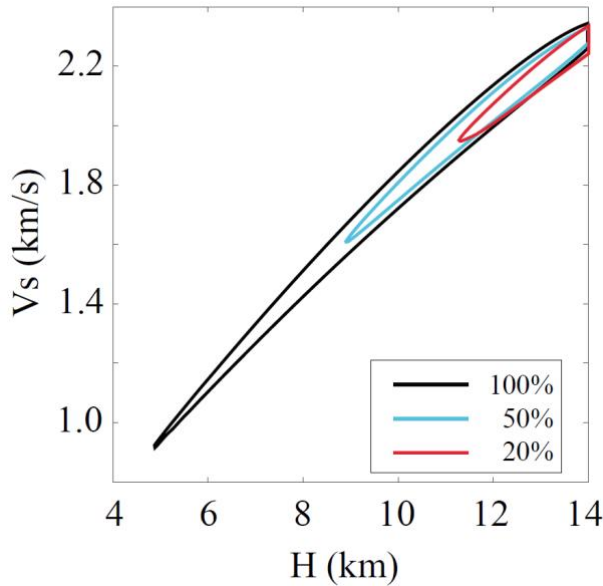
708

709

710 **Figure S3.** S-wave speed models for Layer 1 using single event S0235b.

711 The layout is the same as Fig. 5. An additional ray-theory-based curve (with the delay time of 10.2 s) is included for  
 712 comparison in (b) and (c).

713



714

715 **Figure S4.** Synthetic tests for the influence of different weights.

716 The black, cyan, and red contours are derived from different relative weights (i.e., 100%, 50%, and 20%, respectively)  
 717 of event S0235b in the inversion. For a given depth (e.g., 12 km), the average S-wave speed is smaller for a smaller  
 718 relative weight of S0235b. Note that the acceptable regions (thresholds for relative weights of 100%, 50%, and 20%  
 719 are 0.910, 0.790, and 0.745, respectively) shrink since the signal-to-noise ratio decreases as the relative weights for  
 720 other events increase.

721

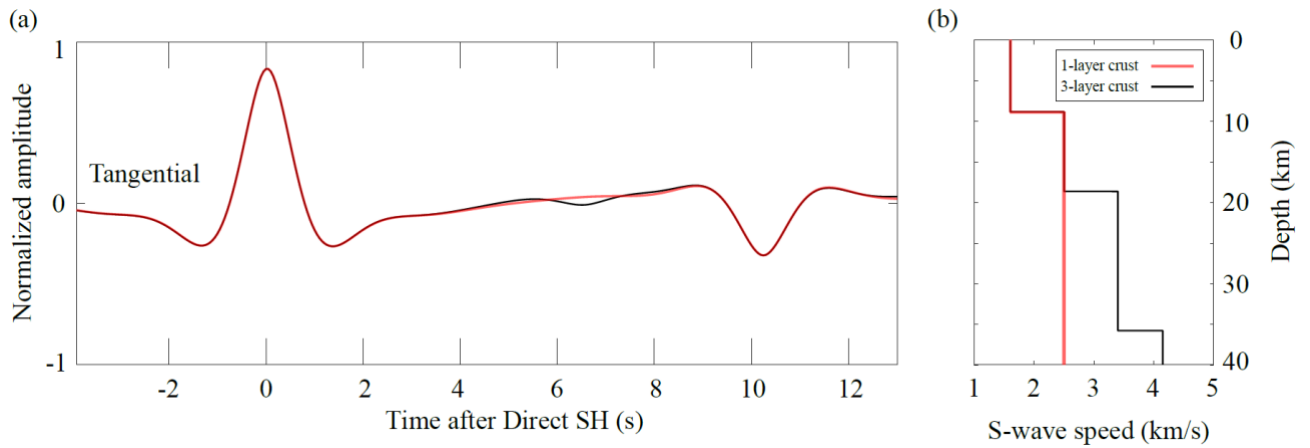
722

723

724

725

726



727

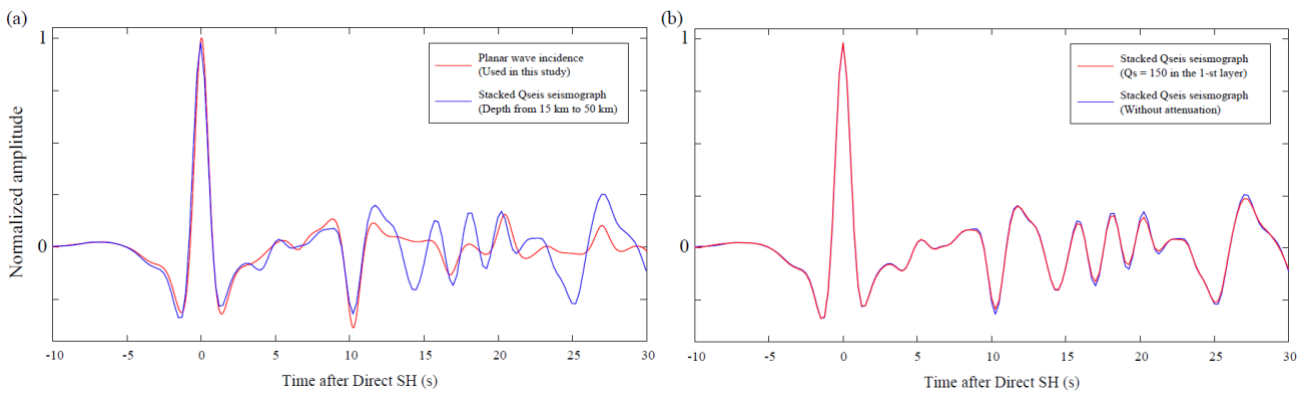
728

729 **Figure S5.** Synthetic tests for the forward modeling setting used in this study.

730 (a) Comparisons between the synthetic SH-wave reflections from a simplified 1-layer crust model (red) and a 3-  
 731 layer crust (black), on the tangential component.

732 (b) Models used for this test. The red and black curves show the 1-layer crust and 3-layer crust models, respectively.

733



734

735

736 **Figure S6.** Synthetic tests for the forward modeling approach used in this study.

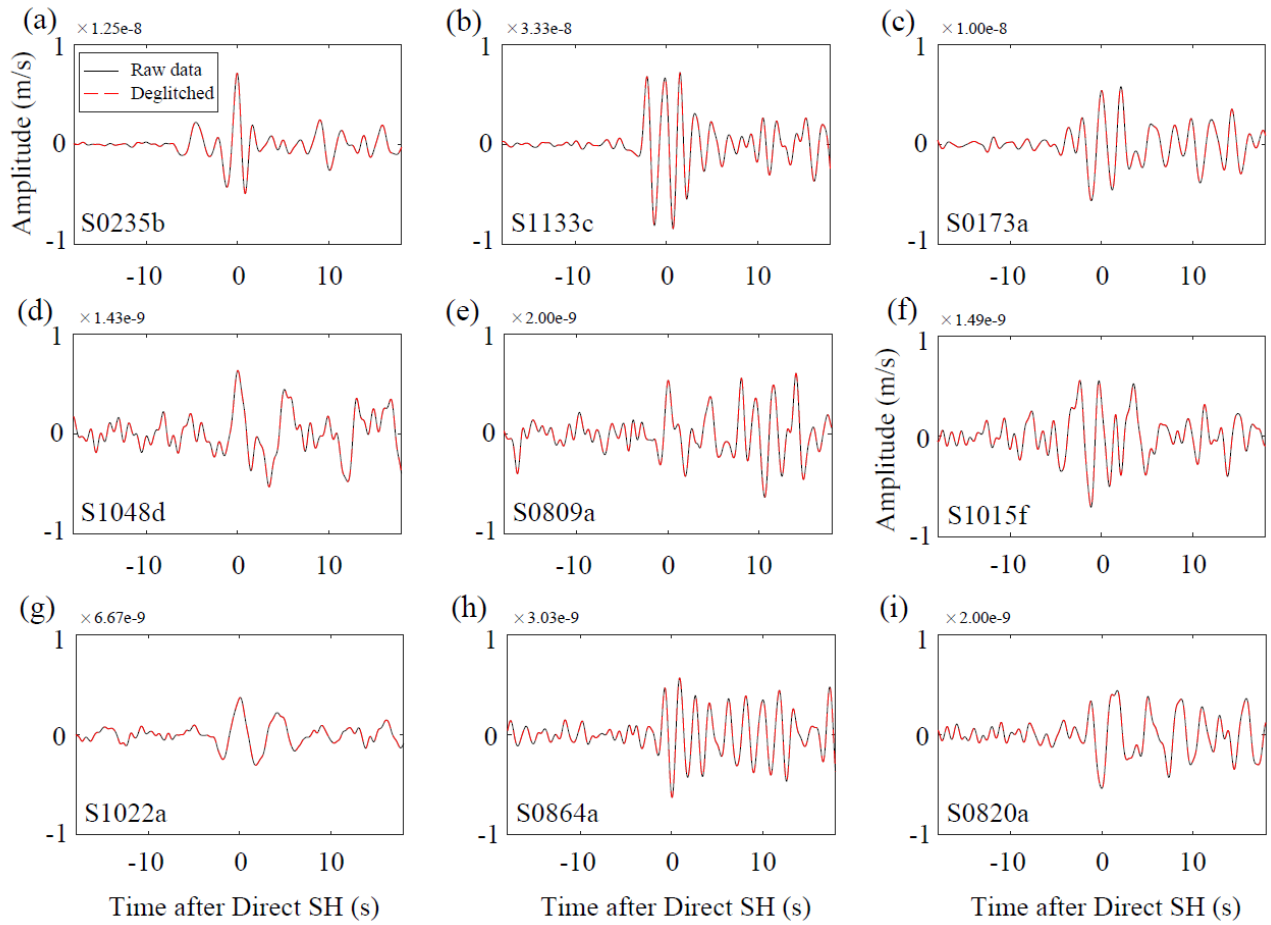
737 (a) Comparison between the waveform calculated with a planar wave incidence (used in this study, red color) and  
 738 the stacked waveform (in blue, where we stacked eight seismograms with depths ranging from 15 km to 50 km  
 739 with an interval of 5 km) calculated using reflectivity code QSEIS (Wang, 1999). Note that the negative signal  
 740 at around 10 seconds is consistent for both methods.

741 (b) Comparison between the waveform without attenuation (in blue) and with strong attenuation in Layer 1 (in red,  
 742 using  $Q_s = 150$ ). Note that the amplitude of the SH-wave reflections is only very slightly influenced by the  
 743 attenuation.

744

745

746



747

748

749 **Figure S7.** Tests for the influence of glitches.

750 (a-i) Comparison between the raw data (solid black) and the deglitched data (dashed red) for all nine quality-A  
 751 marsquakes.

752

753

754

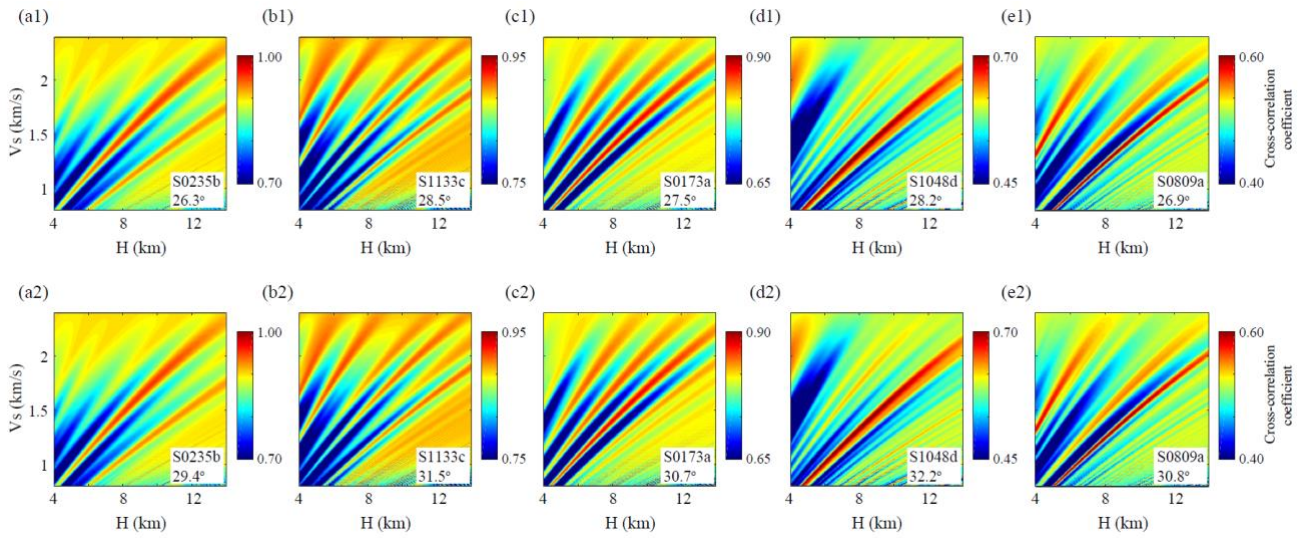
755

756

757

758

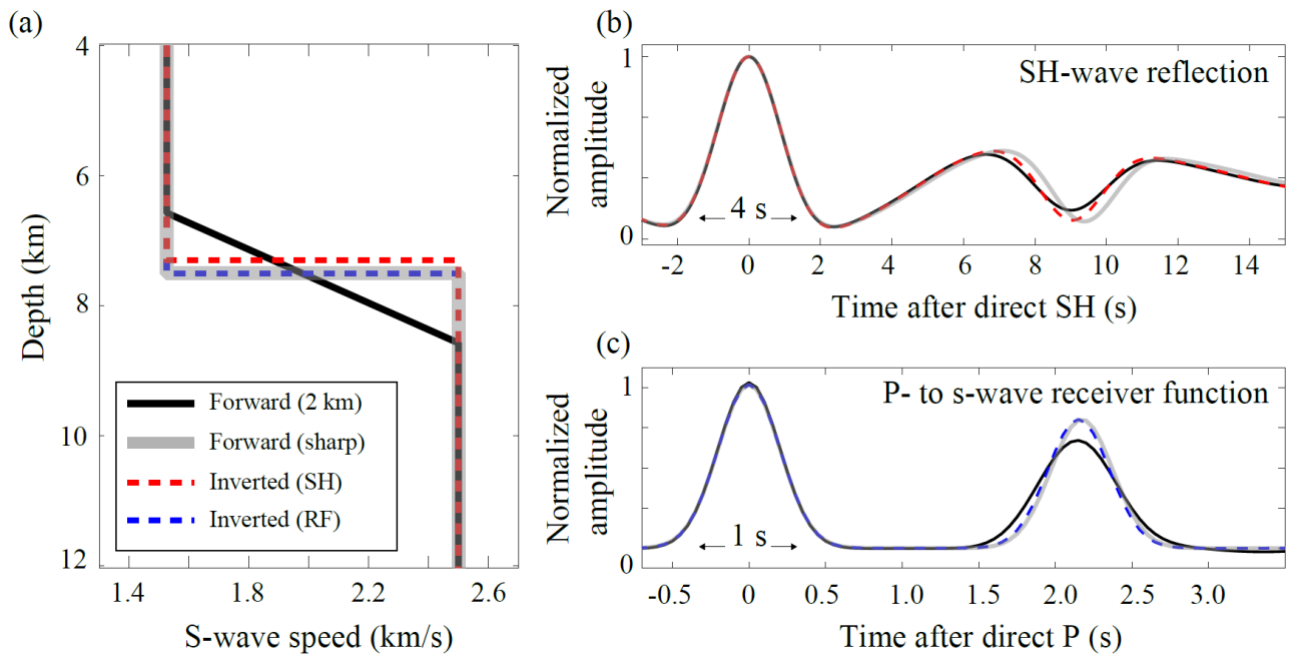
759



760  
761

762 **Figure S8.** Synthetic tests for the influence of the epicentral distance. Cross-correlation map for event S0235b with  
763 a minimum epicentral distance of  $26.3^\circ$  (a1) and a maximum epicentral distance of  $29.4^\circ$  (a2). Similar plots for (b1-  
764 b2) S1133c, (c1-c2) S0173a, (d1-d2) S1048d, and (e1-e2) S0809a.

765  
766  
767  
768  
769  
770  
771  
772  
773  
774  
775  
776



777

778

779 **Figure S9.** Synthetic tests for the sharpness of Layer 1.

780 (a) Input and output models. The solid black model has a gradual interface (centered at 7.5 km with a thickness of 2

781 km). The synthetic waveform predicted by this gradual model is treated as synthetic data for this test. The solid

782 thick grey line is the reference model, with a sharp interface centered at the midpoint of the gradual model. The

783 dashed red and blue lines represent the inverted models (assuming a sharp interface during the inversion), for the

784 SH-wave reflection and the P- to s-wave receiver function cases, respectively. These inverted models are the

785 ones corresponding to the maximum cross-correlation coefficient among all the candidate models resulting from

786 the inversion. Note that while the inverted depth from the receiver function remains at the midpoint depth (7.5

787 km), the inverted depth from the SH-wave reflections is shallower.

788 (b) Synthetic SH-wave reflections. The solid black, solid thick grey and dashed red waveforms correspond to the

789 ground truth model (gradual interface), reference model, and the inverted model (sharp interface), with the same

790 color in (a).

791 (c) Synthetic P- to s-wave receiver functions, the layout is similar to (b). Note that the time axis is stretched for

792 better comparison with (b).

793

794

795

796

797

798

799

800

801

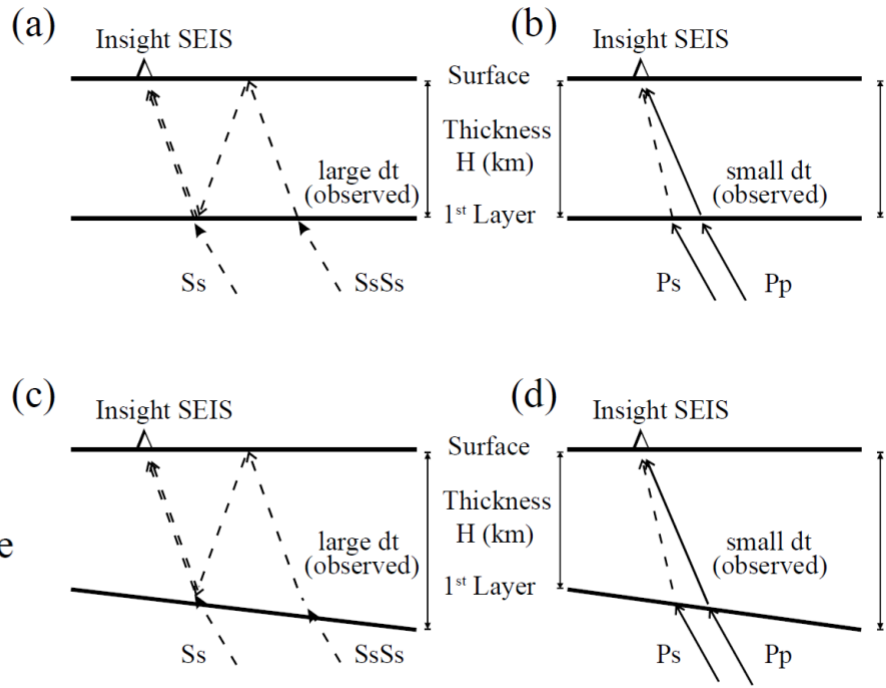
802

803

804

805

$V_{SH} < V_{SV}$   
Flat Interface



806

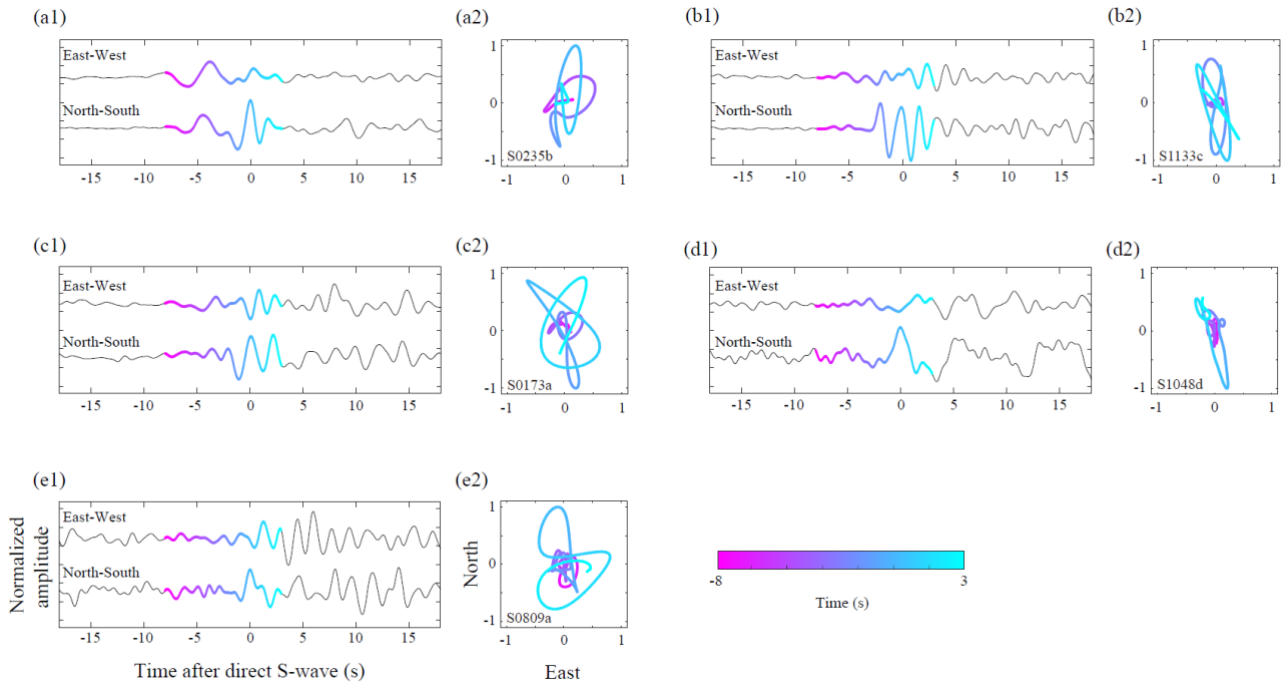
807

**Figure S10.** Schematic ray paths in Layer 1 for SH-wave reflections (a), P- to s-wave receiver functions (b) with a flat interface and negative radial anisotropy. (c-d) Similar plots for ray paths, with a dipping interface but no radial anisotropy.

808

809

810



812

813

814 **Figure S11.** Examination for shear-wave splitting

815 (a1) Raw velocity waveforms on the East-West (at the top) and the North-South (at the bottom) components.

816 (a2) Particle motion analysis for part of the waveforms (-8 to 3 s) on the East-West and North-South components

817 shown in (a1). Colorscales correspond to the arrival time of the traces in (a1).

818 Similar plots for (b1-b2) S1133c, (c1-c2) S0173a, (d1-d2) S1048d, and (e1-e2) S0809a.

819

820

821

822

823

824

825

826

827

828

829

830

831

832

833

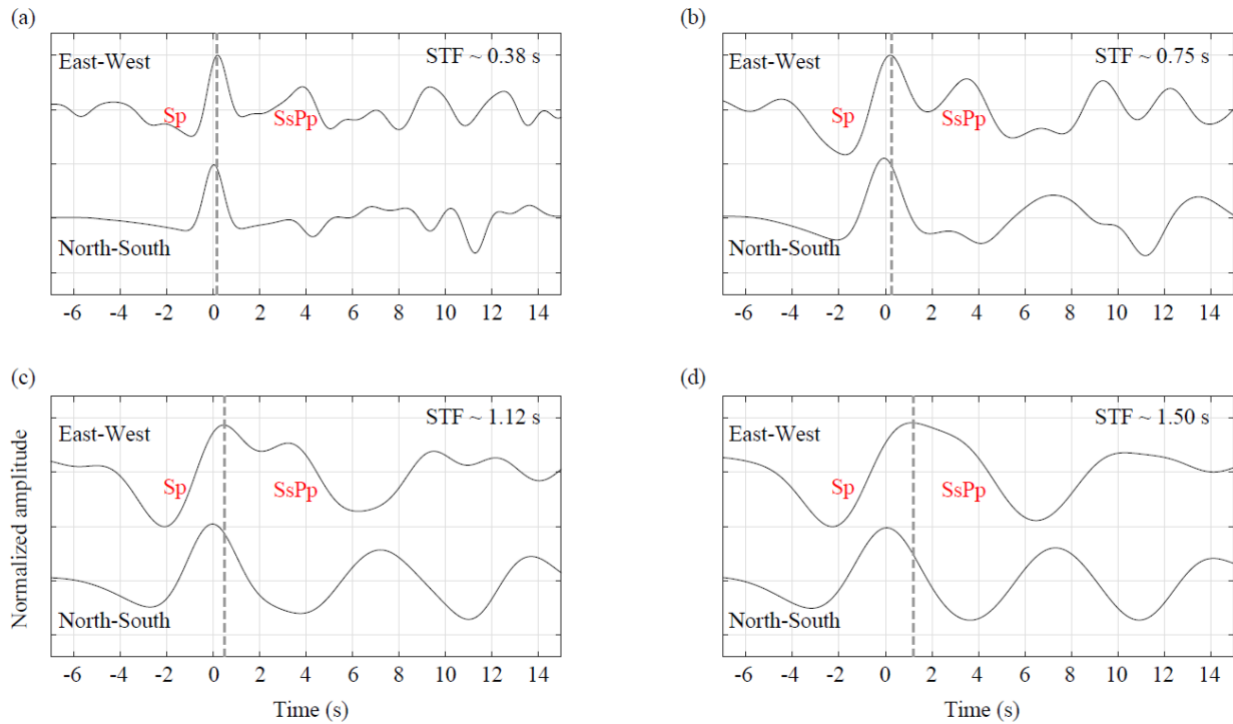
834

835

836

837

838



839

840 **Figure S12.** Synthetic tests for the influence of Sp and SsPp phases.

841 (a) Waveforms on the East-West (at the top) component and the North-South (at the bottom) component with a short  
 842 source time function (Gaussian width of 0.38 s), using orthonormal propagator algorithm, QSEIS (Wang, 1999). The  
 843 Sp and SsPp phases are denoted by red words. The dashed grey line marks the peak location of the direct SV-phase  
 844 (with distortion) on the East-West component.

845 Similar plots for Gaussian width of the source time function of (b) 0.75 s, (c) 1.12 s, and (d) 1.50 s.

846

847

848

849

850

851

852

853

854

855

856

857

858

859

860

861

862

863

864

**Table S1 Events selected for SH-wave reflections**

Event Name	Origin Time (UTC)	Frequency Type	Distance (°)	Back Azimuth (°)	$T_s - T_p$ (s)	$T_{sSs} - T_s$ (s)
<b>S0173a</b>	<b>2019-05-23T02:19:09</b>	<b>Low Frequency</b>	<b>27.9</b>	<b>91</b>	<b>180</b>	<b>10.9</b>
<b>S0235b</b>	<b>2019-07-26T12:15:38</b>	<b>Broadband</b>	<b>26.5</b>	<b>74</b>	<b>167</b>	<b>10.2</b>
<b>S0809a</b>	<b>2021-03-07T11:09:26</b>	<b>Low Frequency</b>	<b>30.8</b>	<b>87</b>	<b>173</b>	<b>10.6</b>
S0820a	2021-03-18T14:51:33	Low Frequency	30.6	88	176	11.2
S0864a	2021-05-02T00:57:35	Broadband	28.5	97	167	10.1
S1015f	2021-10-04T04:52:29	Broadband	27.5	93	160	10.7
S1022a	2021-10-11T23:14:29	Low Frequency	30.7	63	177	10.5
<b>S1048d</b>	<b>2021-11-07T22:00:15</b>	<b>Low Frequency</b>	<b>30.2</b>	<b>100</b>	<b>177</b>	<b>11.7</b>
<b>S1133c</b>	<b>2022-02-03T08:04:36</b>	<b>Broadband</b>	<b>30.0</b>	<b>90</b>	<b>176</b>	<b>10.1</b>

865

866

867 **Table S1.** Events selected for SH-wave reflections. The event name for the five events used in the inversion is in  
868 bold. The optimal values (from InSight Marsquake Service 2020, 2021a, b, 2022a, b) for epicentral distance, origin  
869 time, back azimuth, and differential travel time between P- and S-waves are also included. The measured travel time  
870 differences between the direct SH wave and the SH-wave reflection (from this study) are listed in the last column.

871